A Digital Imaging Technique to Measure Temperatures and Soot Concentrations in Flames of Condensed Phase Fuels

DOT/FAA/TC-21/50

Federal Aviation Administration
William J. Hughes Technical Center
Aviation Research Division
Atlantic City International Airport
New Jersey 08405

December 2021

Final report

U.S. Department of Transportation
Federal Aviation Administration

NOTICE

This report is available at the Federal Aviation Administration William J. Hughes Technical Center's Full-Text Technical Reports page: actlibrary.tc.faa.gov in Adobe Acrobat portable document format (PDF).

Form DOT F 1700.7 (8-72) Reproduction of completed page authorized

1. Report No.	2. Government Accession No.	3. Recipient's Catalog No.
DOT/FAA/TC-21/50		

4. Title and Subtitle	5. Report Date
A Digital Imaging Technique to Measure Temperatures and Soot Concentrations in Flames of Condensed Phase Fuels	December 2021
	6. Performing Organization Code ANG-E21

7. Author(s)	8. Performing Organization Report No.
Haiqing Guo[1], Richard E. Lyon[2]	

9. Performing Organization Name and Address	10. Work Unit No. (TRAIS)
[1]Diakon Solutions, 110 W Beaver Dr., Cape May Court House, NJ 08210 [2]Federal Aviation Administration, William J. Hughes Technical Center, Atlantic City Airport, NJ 08405	11. Contract or Grant No.

12. Sponsoring Agency Name and Address	13. Type of Report and Period Covered
U.S. Department of Transportation FAA Northwest Mountain Regional Office 1601 Lind Avenue SW Renton, WA 98057	14. Sponsoring Agency Code AIR-600

15. Supplementary Notes

16. Abstract

Knowing fire temperature and soot concentration in a fire is very important in fire safety research. The fire radiant energy, a function of fire temperature and soot concentration, contributes about 40% of energy loss to the walls of the Ohio State University (OSU) fire calorimeter during the burning of large area cabin materials. This report presents a method to measure the full field of flame temperature and soot volume fraction in fire using a digital camera. The report also outlines a new procedure to simultaneously calibrate and characterize the camera's detector using a blackbody furnace. The developed methods are implemented to measure flame temperature and soot volume fraction in a liquid-fueled steady laminar diffusion flame, impacted by the phosphorus type flame-retardant material. The flame-retardant material is found to promote soot formation and suppress soot oxidation in the fire. The increased net soot concentration cools the flame, resulting in incomplete combustion.

17. Key Words	18. Distribution Statement
Flame temperature, soot volume fraction, flameretardant material, soot emission	This document is available to the U.S. public through the National Technical Information Service (NTIS), Springfield, Virginia 22161. This document is also available from the Federal Aviation Administration William J. Hughes Technical Center at actlibrary.tc.faa.gov.

19. Security Classif. (of this report)	20. Security Classif. (of this page)	21. No. of Pages	22. Price
Unclassified	Unclassified	55	

Contents

Figures

Acronyms

Acronym	Definition
FAA	Federal Aviation Administration
RGB	Red, green, blue
SLR	Single-lens reflex
MMA	Methyl methacrylate
PMMA	Polymethyl methacrylate
TMP	Trimethyl phosphate
CMOS	Complementary metal–oxide–semiconductor
OSU	Ohio State University

Executive summary

In fire safety research, flame temperature and soot concentration are among the most important measurements. Knowing the soot concentration and temperature allows for the calculation of the radiant energy that is lost to the walls of the Ohio State University (OSU) fire calorimeter during burning of large area cabin materials in Federal Aviaiton Regulations (FAR) 25.853(a-1). This radiant energy can be as much as 40% of the heat released by combustion. FAA's oil burner flammability test in Title 14 Code of Federal Regulations (14 CFR) Part 25.853 uses fire temperature as the criterion to determine if a conducted fire performance test is valid. In this research, an imaging technique is developed to simultaneously measure flame temperature and soot concentration in flames. The technique utilizes the red, green, and blue (RGB) channels of a consumer-grade digital single-lens reflex (SLR) camera as the detector. The imaging system is calibrated and characterized simultaneously with a temperature reference. A customized toolbox is developed to perform imaging-processing and convert the recorded RGB signal to full-field, high-fidelity measurements of flame temperature and soot volume fraction.

As part of this research, a method was developed to create an axisymmetric, quasi-steady, laminar diffusion flame from liquid fuels. The liquid-fueled flame system allows for the addition of soluble flame-retardant chemicals and direct observation of the impact of these on the flame structure, flame temperature, and soot production. Liquid fuels tested include methyl methacrylate (MMA) monomer to emulate the burning of polymethyl methacrylate (PMMA) with and without the addition of a phosphorus-containing flame retardant, trimethyl phosphate (TMP). The phosphorus-containing flame retardants are becoming increasingly important in the aircraft industry due to a recent requirement to phase-out halogenated flame retardant (polybrominated diphenylethers) by the United States Environmental Protection Agency. However, the impact of the phosphorus flame retardants on material flammability and combustion toxicity is controversial and the mechanism of flame-retardancy is not well understood. This research aims to resolve these problems by developing advanced characterization methods for material flammability in support of the FAA regulatory mission to improve the fire safety of aircraft cabin materials.

In this research, a new imaging technique is implemented to measure the flame temperature and soot concentration in the MMA and MMA+TMP flame systems. Results indicate that TMP increases soot production in fires which radiates energy and cools the flame. At the tip of the flame, the low temperature generates a column of soot and other incomplete combustion products, including toxic gases such as carbon monoxide.

1 Introduction

In fire safety research, flame temperature is one of the most critical measurements to evaluate the severity of the burning process. In FAA's fire safety guidelines, flame temperature is often used as a criterion to determine if a conducted fire performance test is valid. For example, the FAA oil burner flammability test for seat cushions (Marker, 2019) in compliance with the requirements of 14 CFR 25.853 requires that the average temperature of thermocouples for flame temperature should be 927 ± 55 °C. In the power-plant fire penetration test (Marker, 2019), it is required that the minimum test flame temperature as measured by the thermocouple is 1093 °C. Flame temperature is also critical in fundamental fire research because it controls the chemical reaction rate, heat release, and flame spread rate. It is known (Guo, Walters, Lyon, & Crowley, 2021) that brominated and phosphorous flame retardants lower the flame temperature, either by reducing the homogeneous gas-phase reaction rate or by a heterogeneous mechanism of increasing soot production (reradiation).

Accurate measurement of the flame temperature is nontrivial. Thermocouples are the most commonly used technique to measure flame temperatures because of their simplicity. However, a thermocouple is a point-measurement technique that does not provide the temperature distribution inside the flame. A radiation correction is required to obtain an accurate flame temperature (Maun, Sunderland, & Urban, 2007). It is found that the radiation correction for a 200 μm diameter thermocouple can be as high as 200 °C in a 1600 °C flame (Shaddix, 2017). In sooty flames, the soot sticks to the thermocouple bead surface and further deteriorates the accuracy and repeatability of the temperature measurement. Researchers have previously measured flame temperature using soot radiation and imaging technology. However, due to the unknown emissivity of soot, direct infrared camera technology cannot be used for flame temperature measurement. Instead, the ratio of the soot radiation signal at different wavelengths (soot ratio pyrometry) is used to cancel out the unknown soot emissivity term in measuring flame temperature. Guo et al. (Guo, Castillo, & Sunderland, 2013) used the narrow-band ratio pyrometry technique to achieve full-field flame temperature measurements in an ethylene/air co-flowing laminar diffusion flame. The measured flame temperature was in the range 1330 – 1580 °C with an estimated uncertainty of less than 50 °C. Kuhn et al. (Kuhn, Ma, Connelly, Smooke, & Long, 2011) directly used the embedded RGB color channel of the digital camera for broad-band ratio pyrometry, and the flame temperature is measured in a single image. This technique requires careful calibration against a temperature reference, an imaging spectrograph, and a scientific camera.

Soot ratio pyrometry can also be used to obtain soot concentration in the flame. In compartment fires, soot increases the radiative heat flux that drives flame spread. Like many other incomplete combustion products, soot can be toxic. Soot also obscures vision in compartment fires, which reduces the evacuation rate in buildings and aircraft cabins.

Soot concentration can be measured by the laser extinction technique (Guo, Castillo, & Sunderland, 2013). In fires where soot radiation is the dominant mechanism of heat exchange, chemiluminescence becomes negligible, and soot concentration can be measured by measuring irradiance if the flame temperature is known. In the work of Guo et al. (Guo, Castillo, & Sunderland, 2013), soot concentration is simultaneously determined from a narrow-band soot emission technique. In the current research, a modified version of the narrow-band soot emission technique is extended to broad-band.

Soot also plays a very important role in the research of flame-retardant materials that are widely used aircraft industry. In recent research by Guo et al. (Guo, Walters, Lyon, & Crowley, 2021), phosphorous flame-retardant material promotes soot formation in fires and decreases the soot surface reactivity. As a result, the decrease in heat release and increase in radiative heat loss is speculated to lower the local flame temperature and also suppress the $CO \rightarrow CO_2$ oxidation process, increasing the yield of carbon monoxide (CO). Unfortunately, the previous research used an unsteady turbulent flame in a fire calorimeter where the flame structure, temperature field, and soot concentration field constantly change. For accurate soot and flame temperature measurements locally and globally, it is important to have a steady-state (static) flame.

Researchers have used mixed-gas flames with and without flame retardants to obtain static flames. For example, Korobeinichev et al. (Korobeinichev, Bolshova, Shvartsberg, & Chernov, 2001) used a methane-air mixture containing a flame retardant and measured flame temperatures. Unfortunately, flame retardant's impact on soot is not explored and the composition of fuels that are gaseous at ambient temperature is limited and very different from the liquid fuels generated by the burning polymers at pyrolysis temperatures (300 °C-500 °C). Raffan-Montoya et al. (Raffan-Montoya, Ding, Stoliarov, & Kraemer, 2015) developed a milligram-scale flame calorimeter that generates a laminar diffusion flame of pyrolysis products using controlled heating to high temperature. The pyrolyzed fuel is mixed with methane to generate a diffusion flame containing flame-retardant species. However, the diffusion flame is unsteady (time-varying) and unsuitable for measuring static temperature and composition profiles.

As discussed above, flame temperature and soot concentration measurements are currently limited to gaseous fuels. Consequently, research was conducted to extend these measurements to

condensed phase (liquid/solid) fuels to better understand the effect of flame-retardant chemicals on the fire hazard of plastics used in aircraft cabin materials:

- Develop an imaging system to allow high-fidelity, full-field measurement of flame temperature and soot volume fraction using a consumer-grade digital camera.
- Calibrate and characterize the image detector to improve measurement accuracy.
- Develop an image-processing toolbox to automate the measurement.
- Develop a liquid fuel delivery system that will accommodate flame retardant chemicals and generate a steady laminar diffusion flame.
- Implement the imaging technique to measure flame temperature and soot volume fraction locally and globally to reveal mechanisms of flame inhibition by chemicals used to reduce the flammability of solid plastics.

2 Theory

This section provides detailed theory and derivation steps underlying the imaging technique used in this research. Both the narrow-band soot ratio pyrometry and the broad-band soot ratio pyrometry for temperature measurement are introduced. The theory for soot volume fraction measurement is also presented.

2.1 Narrow-band soot ratio pyrometry

Spectral radiance W_λ emitted by a material can be obtained following Planck's law:

$$W_\lambda = \varepsilon B_\lambda = \frac{2hc^2\varepsilon}{\lambda^5[\exp(hc\ /\ \lambda kT) - 1]} \quad (1)$$

where B_λ is the ideal blackbody spectral radiance, c is the speed of light, h is Planck's constant, k is Boltzmann's constant, T is temperature, λ is wavelength, and ε is emissivity. The spectral radiance is often correlated with detector's signal, I, following:

$$I = KW_\lambda \quad (2)$$

where K is a constant (for a linear response system) that accounts for transmissivity, bandwidth, view factor, detector sensitivity, etc. The above equations are often implemented in infrared cameras to measure the surface temperature of planar objects which emissivity, ε, is known or can be estimated.

In fires, soot particle also emits light following Planck's law; however, the soot particle emissivity is a complex function that depends on soot concentration, particle morphology, soot composition, etc. In addition, soot also absorbs radiance as light passes through fire (also called self-absorption). The line-of-sight integrated radiance of soot is projected on a detector, according to (Snelling, Thomson, Smallwood, & Gulder, 2002):

$$I(x) = K\int_{-\infty}^{\infty} K_{abs}(x,y)B_{\lambda}(x,y)\exp\left[-\int_{y}^{\infty} K_{ext}(x,y')dy'\right]dy \quad (3)$$

K_{abs} and K_{ext} are the soot absorption and extinction coefficients, x is the coordinate along the detector's imaging plane, and y is the coordinate perpendicular to the imaging plane. Primes denote the integration variable. In laminar diffusion flames with sufficiently short residence time, the soot particle diameter is in a typical range of 20 – 50 nm; so Rayleigh scattering is assumed for soot particles. It is also assumed that the absorption and extinction coefficients of soot are equal (Snelling, Thomson, Smallwood, & Gulder, 2002):

$$K_{abs} = K_{ext} = 6\pi E(m)f_v/\lambda \quad (4)$$

where $E(m)$ is the refractive index absorption function and f_v is the soot volume fraction. In optically thin flames, the exponential term that accounts for self-absorption in Equation 3 is negligible. It is also shown in Equation 4 that soot emissivity is proportional to soot volume fraction and inversely proportional to wavelength. Comparing signal intensity at two distinct wavelengths (λ_1 and λ_2) yields:

$$\frac{I_1(x,y)}{I_2(x,y)} = \frac{\dfrac{K_1 2hc^2 6\pi E(m)f_v}{\lambda_1^6[\exp(hc\,/\,\lambda_1 kT)-1]}}{\dfrac{K_2 2hc^2 6\pi E(m)f_v}{\lambda_2^6[\exp(hc\,/\,\lambda_2 kT)-1]}} \quad (5)$$

Equation 5 can be reorganized and simplified to:

$$T = \frac{hc(1/\lambda_2 - 1/\lambda_1)}{k\ln\left[\dfrac{I_1(x,y)K_2\lambda_1^6}{I_2(x,y)K_1\lambda_2^6}\right]} \quad (6)$$

In Equations 5 and 6, $I_1(x,y)$ and $I_2(x,y)$ are deconvolved local soot irradiance as recorded by the detector at two wavelengths λ_1 and λ_2. Temperatures can be experimentally measured using two band-pass optical filters having center wavelength at λ_1 and λ_2, following Equation 6. With ratio, the soot volume fraction term, f_v and refractive index absorption term, $E(m)$ are canceled out so that the determination of flame temperature does not require knowing f_v and $E(m)$. However, this technique requires a changeover of optical filters during measurements and a steady flame system.

2.2 Broad-band soot ratio pyrometry

Alternatively, researchers utilize the embedded complementary metal–oxide–semiconductor (CMOS) sensor of a digital SLR that can record signals at three color channels: red, green, and blue, simultaneously. Each channel has a broad-band optical filter with the spectral response η_λ as a function of λ. Equation 2 is rewritten by replacing K with $K' \eta_\lambda$:

$$I_\lambda = K' \eta_\lambda W_\lambda \tag{7}$$

Integrating Equation 7 over the detection wavelength yields the detected signal intensity of each RGB channel. The signal intensity S_j of each color channel j ($j = R, G, B$) for a planar object is (Kuhn, Ma, Connelly, Smooke, & Long, 2011):

$$S_j = K' \int \frac{\eta_{j,\lambda} 2hc^2 \varepsilon}{\lambda^5 [\exp(hc \,/\, \lambda kT) - 1]} d\lambda \tag{8}$$

And the signal intensity S_j for soot is:

$$S_j = K' \int \frac{\eta_{j,\lambda} 2hc^2 6\pi E(m) f_v}{\lambda^6 [\exp(hc \,/\, \lambda kT) - 1]} d\lambda \tag{9}$$

Similar to the narrow-band technique, the ratios of intensity signal can also be applied on any pair of channels. For a planar object, there is:

$$\frac{S_{j1}}{S_{j2}} = \frac{\int \frac{\eta_{j1,\lambda}}{\lambda^5 [\exp(hc \,/\, \lambda kT) - 1]} d\lambda}{\int \frac{\eta_{j2,\lambda}}{\lambda^5 [\exp(hc \,/\, \lambda kT) - 1]} d\lambda} \tag{10}$$

And for soot:

$$\frac{S_{j1}}{S_{j2}} = \frac{\int \frac{\eta_{j1,\lambda}}{\lambda^6[\exp(hc\ /\ \lambda kT) - 1]}\, d\lambda}{\int \frac{\eta_{j2,\lambda}}{\lambda^6[\exp(hc\ /\ \lambda kT) - 1]}\, d\lambda} \quad (11)$$

It should be noted that in Equation 11 for soot, wavelength, λ, has a power of 6 instead of 5 as in Equation 10 for a planar object, which accounts for the soot emissivity's inverse proportional relationship with λ. Unlike the exact solution of Equation 5 in Equation 6, Equations 10 and 11 do not have an exact solution for temperature. Alternatively, the relationship between S_{j1} / S_{j2} and T can be tabulated, if the detector's spectral response, η_λ is known.

2.3 Soot volume fraction

The soot emission involves soot volume fraction as shown in Equation 4. Once soot temperature is determined from ratio pyrometry, the soot volume fraction can be determined by combining Equations 1 - 4:

$$f_v = \frac{I\lambda^6[\exp(hc\ /\ \lambda kT) - 1]}{12\pi hc^2 KE(m)} \quad (12)$$

As shown in Equation 12, calculation of soot volume fraction requires knowledge of the optical constant K and the refractive index absorption function $E(m)$. The optical constant could be obtained by calibrating the optical system against a blackbody furnace with known emissivity and controllable temperature. The soot refractive index absorption function is expressed as:

$$E(m) = -IM\left(\frac{m^2 - 1}{m^2 + 2}\right) \quad (13)$$

where m is the soot refractive index having the form of $m = a - bi$. The real part a accounts for light scattering and the imaginary part b accounts for light absorption. And IM is a math operator that takes the imaginary part of the results. Plugging m into Equation 13 yields:

$$E(m) = \frac{6ab}{(a^2 - b^2 + 2)^2 + 4a^2b^2} \quad (14)$$

In the current research, a refractive index of $m = 1.57 - 0.56i$ is assumed (Dalzell, Williams, & Hottel, 1970), which yields a refractive index absorption function of $E(m) = 0.26$.

3 Experiment

In this section, the experimental setups for the imaging system and the flame system are introduced. Detailed procedures on how to process the signal as recorded by the imaging system are also presented.

3.1 Imaging system

The detector (imaging system) used in the current study is a consumer-grade digital SLR camera, Nikon D750. The camera is equipped with a 36 × 24 mm full-frame format CMOS sensor with 24.3 megapixels (6032 × 4032 pixels) and 14-bit depth in each of the three color channels. The camera is also equipped with a 24 – 120 mm AF-S Nikkor lens. In experiments, the camera's focal length is fixed at 120 mm.

All settings of the camera, except the shutter speed, are kept the same in all experiments and calibrations. Shutter speed is optimized for each image such that no pixels are saturated in any color channel. All automatic exposure and image post-processing options are disabled. The aperture is set to f / 10, the ISO is 100, and the white balance setting is direct sunlight. The sensor plane is kept 2 m away from the imaging object. Focus is manually adjusted to obtain the sharpest image of the object. In both calibration and fire experiments, the room light is turned off to minimize background interference.

3.2 Flame system

This research studies a liquid-fueled jet laminar diffusion flame. A 10-mm diameter plug, cut from a 12.7-mm thick ceramic insulation board, serves as a wick. The wick is placed inside a 10-mm diameter copper tube. Outside is a concentric 100 mm inside diameter aluminum tube. The volume between two tubes creates a flow path for air. A 1.5-mm cell-size 50-mm thick ceramic honeycomb is placed in between the two concentric tubes to obtain plug coflow. The airflow rate is maintained at 850 mg/s to straighten and stabilize the flame.

Liquid MMA monomer was used as fuel in this flame system to emulate the burning of PMMA. To understand phosphorus flame retardant's impact on the flame structure, trimethyl phosphate (TMP) is added to the MMA to form an MMA+TMP mixture with 2% mass fraction of TMP. Before the beginning of each test, the wick is soaked with pure MMA monomer or MMA+TMP mixture. Once ignited, the flame can maintain a constant flame height for longer than 30 s.

3.3 Image-processing

Images are initially saved in uncompressed Nikon-specific format. It should be noted that all consumer-grade cameras apply a nonlinear operation, gamma correction, to accommodate the nonlinear human eye behavior. The gamma corrections need to be removed for scientific measurements in this study so that the linear response assumption (a constant K in Equation 2) is justified. The conversion of raw image files to tiff format is performed using the open-source program dcraw (Coffin, 2021). The decode settings are: "−4" for non-gamma-corrected linear output, "−T" for tiff output, and "−o 0" for raw color space. Three color planes at each pixel of the image are extracted using the tifffile module in Python. The signal intensity is normalized by the camera shutter speed.

3.3.1 Smoothing

A customized image-processing toolbox developed with Python programming language is used to process the flame images. The toolbox scans the flame image at each height above the wick tip and extracts the normalized intensity signal. Vertically (along the flame height direction), the pixel intensity is averaged across a 0.5 mm range, assuming the flame properties do not change much within 0.5 mm. The vertically averaged information is stored every 1 mm (vertical spatial resolution). At each height, linear fitting is performed on both sides to generate the baseline. The baseline is subtracted to further minimize the background noise. Horizontally (perpendicular to the flame height direction), a second-order Savitzky-Golay filter with a window size of 11 is applied to further smooth the data. The appropriate values of filter order and window size are chosen such that the peak information is not suppressed.

In the current research, the flame properties are assumed to be axisymmetric along the center axis. At each flame height, an optimization algorithm is implemented to locate the flame center point. The center point is identified as the point where the Euclidian distance between the flipped (about the point) left-side signal and the right-side signal is minimal.

3.3.2 Deconvolution

The irradiance intensity from a flame is three-dimensional. With the camera technique used in this research, the 3D information is flattened to 2D; and each recorded pixel contains line-of-sight integration of information along the axis perpendicular to the imaging plane. For better accuracy, deconvolution is required to reconstruct the local irradiance of the flame.

The deconvolution is sufficiently simplified when the flame is axisymmetric. Figure 1 illustrates the algorithm of the onion-peeling type deconvolution (Guo, 2015). In an axisymmetric flame,

the cross-section at any flame height can be taken as one axisymmetric 2D plane. The entire domain can be divided into a series of concentric rings. The properties within each ring are assumed to be constant. At the outmost cord, x_{i+1}, all the properties are within the same ring, so its line-of-sight integration value at the projection plane can be expressed as $P(x_{i+1}) = F(\xi_{j+1})\ l_{i+1,j+1}$, where $F(\xi_{j+1})$ is the local property at the outmost ring j+1, and $l_{i+1,j+1}$ is the integration length at x_{i+1} (blue line at x_{i+1} as indicated in Figure 1). Local property $F(\xi_{j+1})$ can be calculated first. At cord x_i next to x_{i+1}, the projection is expressed as: $P(x_i) = F(\xi_{j+1})\ l_{i,j+1} + F(\xi_j)\ l_{i,j}$. Here, $F(\xi_j)$ is the local property at ring j, and $l_{i,j+1}$ is part of the integration length at x_i (blue line at x_i as shown in Figure 1) and $l_{i,j}$ is another part of the integration length at x_i (red line at x_i as shown in Figure 1). Now the local property $F(\xi_j)$ can be calculated by plugging the calculated $F(\xi_{j+1})$ value. Following this procedure, the next ring's property can be calculated with a known $F(\xi_{j+1})$ and $F(\xi_j)$.

A more general expression of the onion-peeling deconvolution is (Guo, 2015):

$$F(\xi_j) = \sum_{i=j}^{R} [s_{ji}]^{-1} P(x_i), \quad r_j < \xi_j < r_{j+1} \tag{15}$$

where s_{ji} is a matrix of the length of the i-th cord in the j-th ring:

$$\begin{aligned} s_{ji} &= 2\left(\sqrt{r_{j+1}^2 - x_i^2} - \sqrt{r_j^2 - x_i^2}\right) \\ &= 2\left(\sqrt{[x_i + \Delta(j-i+1)]^2 - x_i^2} - \sqrt{[x_i + \Delta(j-i)]^2 - x_i^2}\right) \end{aligned} \tag{16}$$

Here, r is the radius and R is integration limit of r, and Δ is spatial resolution.

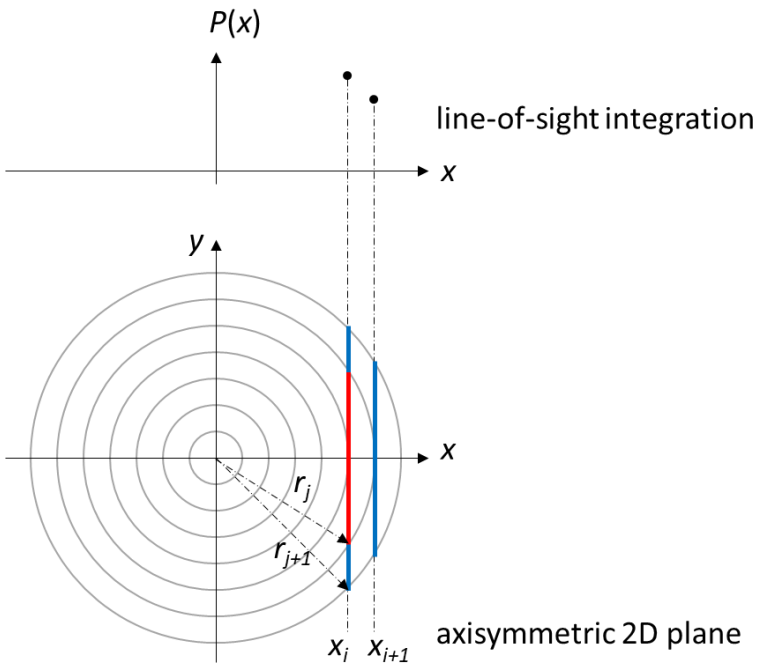

Figure 1. Illustration of the onion-peeling deconvolution algorithm

The above onion-peeling method based on numerical approximation is for illustration purposes. A more accurate analytical solution, Abel transform, is used in the current research. The Abel transform algorithm is implemented in Python, following (Hughey & Santavicca, 1982):

$$F(r_i) = \frac{-2}{\pi} \sum_{j=i}^{R-1} \frac{P(j-1) - P(j)}{r_{j+1}^2 - r_j^2} \left[\sqrt{r_{j+1}^2 - r_i^2} - \sqrt{r_j^2 - r_i^2} \right] \quad (17)$$

3.3.3 Temperature and soot volume fraction calculation

The blue channel has the lowest signal intensity among all three channels. For higher signal/noise ratio, only the red and the green channels are used. The temperature is calculated from the pair of red/green channels. A threshold of 0.2 is applied to cutoff any deconvolved value lower than 20% of the maximum value. The ratio of the deconvolved red channel intensity and the deconvolved green channel intensity is calculated for each radial location, and its corresponding temperature is determined with a calibration curve that directly correlates

temperature with the signal ratio (see Equation 11). The details of the calibration will be described in the next section.

Once the temperature is determined for each radial location, the calculated temperature is plugged into Equation 12 to calculate soot volume fraction at the same location. It is noted that Equation 12 is derived for the narrow-band technique where the wavelength length (λ) can be approximated as a constant. In this research with a broad-band technique, an equivalent wavelength of the color channel must be pre-determined. Details on how to calculate the equivalent wavelength will be described later. In this research, only the red color channel is used for soot volume fraction determination because it has the highest signal/noise ratio.

4 Calibration and characterization

As discussed in the theory section, accurate temperature measurement requires knowing: the linearity response of the imaging system, and the spectral response η_λ of each color channel. Accurate soot volume fraction measurement further requires knowing the optical constant K. The imaging system needs to be calibrated against a temperature reference. This section describes the procedures to calibrate the imaging system and to obtain the optical parameters with a blackbody furnace.

Among all optical parameters, the spectral response would normally require a sophisticated imaging spectrograph (Kuhn, Ma, Connelly, Smooke, & Long, 2011). In this research, different approaches (inversed method, equivalent wavelength method, and optimized Gaussian profile method) are developed and examined. To find the best method to calculate the spectral response, the calibration procedure is first simulated with a prescribed spectral response. And the simulated blackbody radiance captured by the sensor is used to calculate the spectral response using the proposed methods. The calculated spectral response is compared with the prescribed spectral response. The optimal method is selected and implemented using the blackbody furnace experiment data.

4.1 Blackbody calibration

A blackbody furnace (Oriel 67032) is used to calibrate the imaging system and to confirm linear camera response. The furnace had a 25 mm cavity opening, an emissivity of $\varepsilon = 0.99 \pm 0.01$, and a temperature accuracy of 0.1 °C. Images of the furnace at temperatures of 900 °C – 1200 °C with an increment of 25 °C were recorded using the camera. The lens was focused on the furnace opening, which was 2 m from the CMOS sensor. The recorded blackbody irradiance at each color plane is plotted against the blackbody furnace temperature as shown in Figure 2.

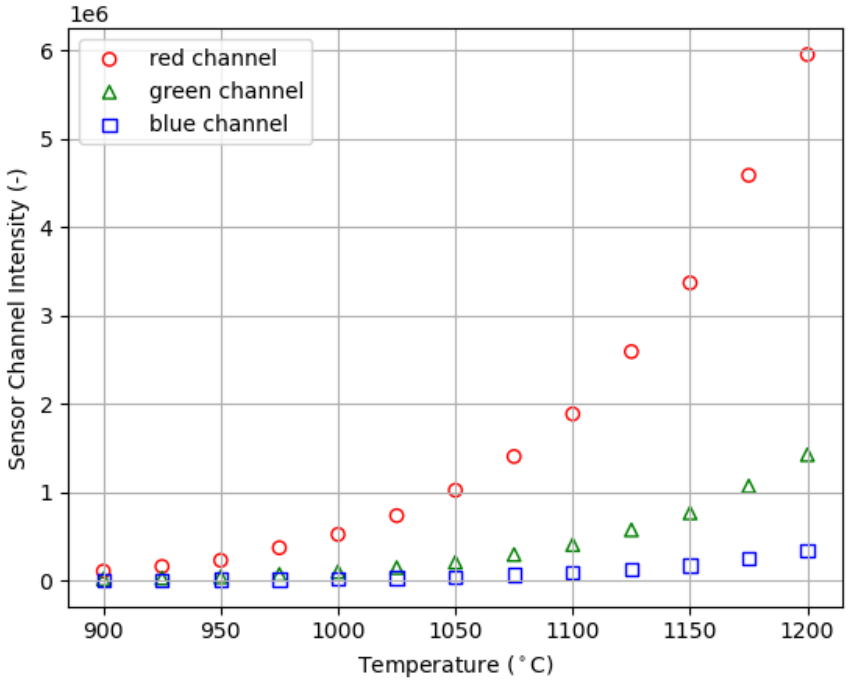

Figure 2. Recorded blackbody furnace irradiance at detector's RGB color channel

Spectral radiance of the blackbody furnace is calculated using Equation 1 with the emissivity of the blackbody furnace $\varepsilon = 0.99$. The calculated spectral radiance can be plotted against the measured color channel intensity to examine the imaging system linearity and to calculate the optical constant K'. Figure 3 shows the red channel calibration results. Linear-fitting (through origin) of the data yields an optical constant of $K' = 0.03239$. The coefficient of determination (R^2) is nearly 1, indicating the imaging system has high linearity.

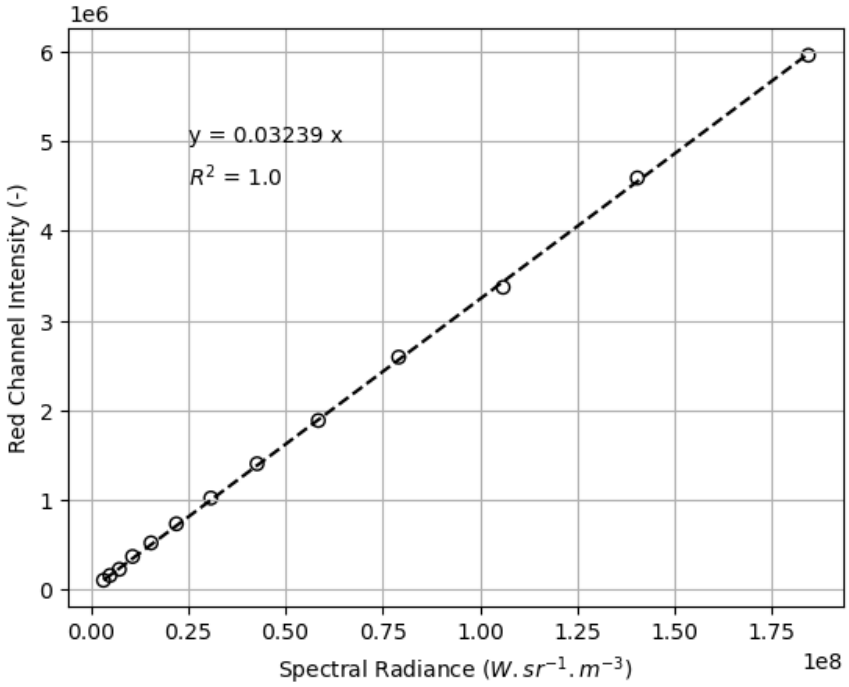

Figure 3. Linearity spectral response of the red channel

4.2 Simulation using prescribed detector spectral response

In the simulation part, it is assumed that the spectral response is known. Here, an arbitrary RGB spectral response is prescribed, as shown in Figure 4.

The prescribed spectral responses are indicated in solid lines. The ideal signal intensity detected of the blackbody furnace at each calibration temperature is simulated using Equations 1 and 7. Next, the developed methods (inversed method, equivalent wavelength method, and optimized Gaussian profile method) will use the simulated signal intensity as input to calculate the spectral response of the color channels. The calculated spectral response will be compared with the prescribed spectral response for validation.

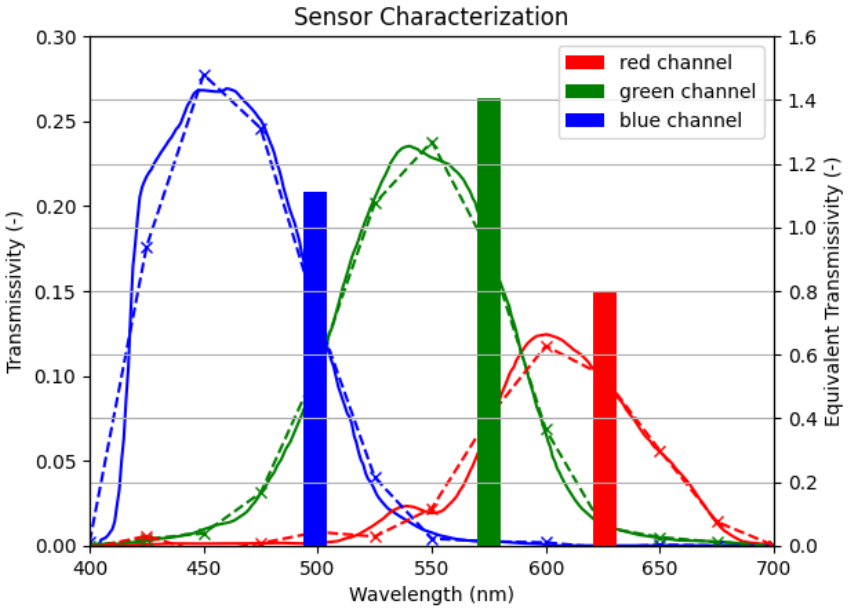

Figure 4. Prescribed spectral response (solid line), inversed spectral response (dash line), and equivalent wavelength (bar) of the RGB color channel

4.2.1 Inversed method

The spectral response of each color channel can be discretized with a 1 nm increment between the visible wavelength of 400 – 700 nm (in total 300 wavelengths). In blackbody calibration, the temperature setting is also discretized with 25 °C increments between 900 °C – 1200 °C (in total 13 temperatures). Equation 8 can be rewritten in a matrix operation form:

$$[S(T)] = K'[W(T,\lambda)] \cdot [\eta(\lambda)]\Delta\lambda \tag{18}$$

Here $[S(T)]$ is a 13 × 1 array, K' is a constant, $[W(T,\lambda)]$ is a 13 × 300 matrix, $[\eta(\lambda)]$ is a 300 × 1 array, and $\Delta\lambda$ is the wavelength increment.

To make Planck's function matrix $[W(T,\lambda)]$ invertible, the size of the matrix in the wavelength direction needs to be down-sampled. Therefore, Equation 18 becomes:

$$[S(T)] = K'[\bar{W}(T,\lambda)] \cdot [\bar{\eta}(\lambda)]\Delta\lambda \tag{19}$$

The down-sampled Planck's function matrix $[\bar{W}(T,\lambda)]$ is a 13 × 13 matrix, and the down-sampled spectral response $[\bar{\eta}(\lambda)]$ is a 13 × 1 array. Multiplying both sides of Equation 19 by the inverse of Planck's function, $[\bar{W}(T,\lambda)]^{-1}$ yields:

$$[\bar{\eta}(\lambda)] = [\bar{W}(T,\lambda)]^{-1}[S(T)]/K'\Delta\lambda \quad (20)$$

The calculated $[\bar{\eta}(\lambda)]$ for each color channel using Equation 20 is also shown in Figure 4, indicated as a dashed line. Despite the low resolution due to down-sampling, the calculated spectral response agrees well with the prescribed spectral response (solid line).
This inversed method is promising because of its simplicity. However, the Planck's function matrix is ill-conditioned, making the spectral response $\bar{\eta}(\lambda)$ calculation very sensitive to signal intensity input $S(T)$. To justify that, a random perturbation between ± 0.5%, which is typical for a digital camera's noise level, is applied to the signal intensity input $S(T)$. The calculation of the spectral response using Equation 20 yields nonsense results.

4.2.2 Equivalent wavelength method

The equivalent wavelength method assumes there exists an equivalent wavelength (λ_e) and equivalent transmissivity (η_e) for each color channel. Equation 8 can be rewritten as:

$$\eta_e d\lambda = [S(T)]/[W(T,\lambda_e)] \quad (21)$$

For each candidate equivalent wavelength, the calculated equivalent transmissivity is a function of furnace temperature. It is noted that the optical property should be independent of temperature. Therefore, the appropriate value of the equivalent wavelength is chosen such that the relative standard deviation of the calculated ηe is minimal. Figure 5 plots the relative standard deviation of equivalent transmissivity among 13 blackbody furnace temperature settings at each wavelength. The identified equivalent wavelength of each color channel is also marked in Figure 4.

It is noted that the equivalent wavelength of each color channel is located at the right side (higher wavelength) of its spectral response peak. This is because, in the explored temperature range, blackbody's spectral radiance monotonically increases with wavelength. The detected signal at a higher wavelength can be higher despite that its transmissivity is slightly lower.

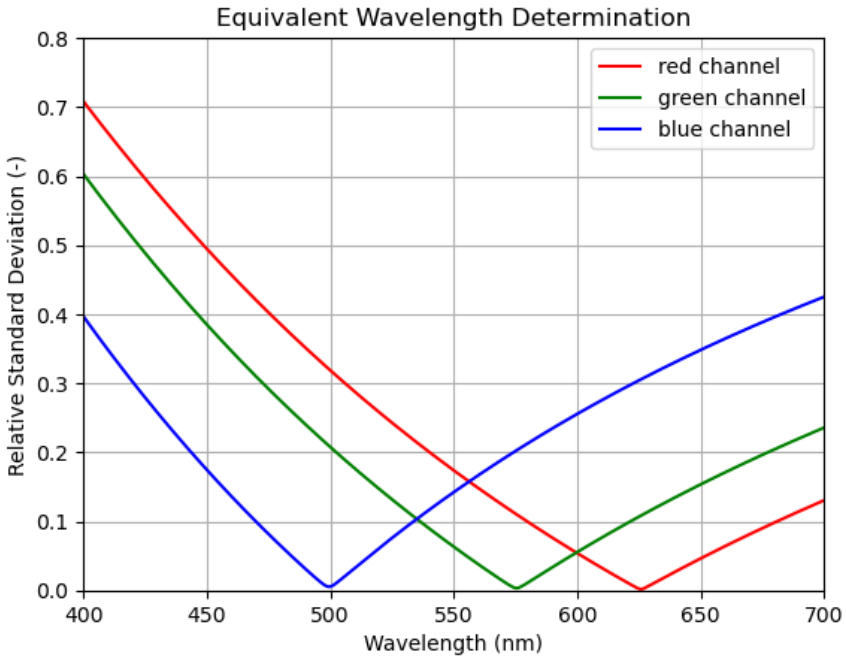

Figure 5. Relative standard deviation of the equivalent filter transmissivity

The calculated equivalent wavelength and equivalent transmissivity can be plugged into Equation 10 to calculate the signal intensity ratio of the blue/green, blue/red, and green/red pairs. The prescribed spectral response (real filter) is also plugged in Equation 10 and marked as dotted lines. Figure 6 shows the ratios of simulated blackbody irradiance on the color channel pairs, marked as open circles. It is seen that within the calibration temperature range, the equivalent wavelength performs as good as the prescribed spectral response. At temperatures higher than the calibration range, there exists a slight discrepancy. The discrepancy increases as the temperature increases. Take the G/R channel as an example, the temperature can be off by about 50 °C when the G/R ratio is 0.9.

For soot in flames, calculated equivalent wavelength and equivalent transmissivity are plugged into Equation 11 to calculate the signal intensity ratio of the blue/green, blue/red, and green/red pairs. The results are marked as a dashed line in Figure 7. Also shown in Figure 7 are the blackbody temperature results (solid line). The flame temperature results are notably different from the blackbody temperature results because of soot emissivity's dependence on wavelength.

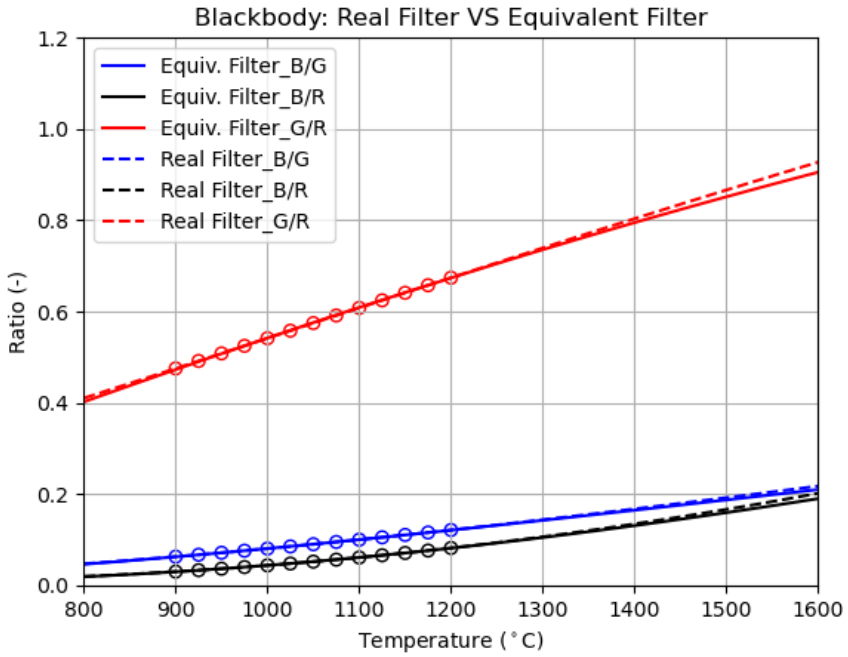

Figure 6. Correlation of blackbody furnace temperature with channel signal ratio using prescribed spectral response (dash line) and equivalent wavelength (solid line)

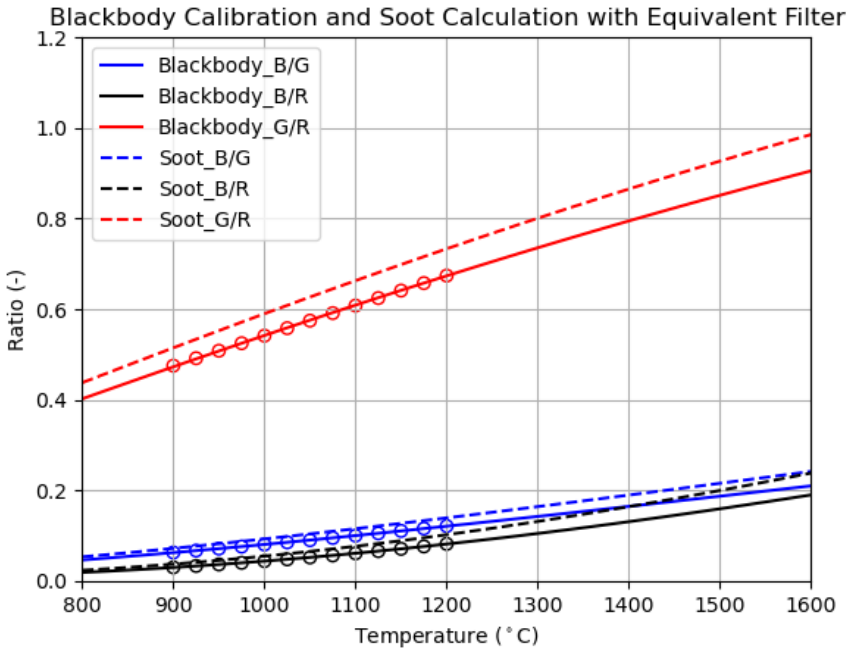

Figure 7. Correlation of blackbody furnace temperature (and soot temperature) with channel signal ratio using the equivalent wavelength method

4.2.3 Gaussian profile method

Figure 4 shows that the spectral response of the digital camera's detector typically has a Gaussian function profile. In this method, a Gaussian function is used to approximate the detector's spectral response:

$$\eta_G(x) = a \cdot \exp\left[-\frac{(x-b)^2}{2c^2}\right] \qquad 22$$

The constants *a*, *b*, and *c* define the shape of a bell curve. The Gaussian function is plugged into Equations 1 and 7 to simulate the signal intensity at each color channel, and the simulated signal intensity is compared with that from simulation using the prescribed spectral response. The appropriate values of constants *a*, *b*, and *c* are determined by minimizing the difference in comparing the simulated signal intensity. The optimization procedure is performed in Python using the genetic algorithm.

Figure 8 shows the optimized Gaussian function profile. Also included for comparison are the prescribed spectral response and the equivalent wavelength. The Gaussian profile agrees with the prescribed spectral response fairly well. It is seen that for each color channel, the agreement on

the shape's right side is better than that of the left side, due to the higher blackbody irradiance at a higher wavelength.

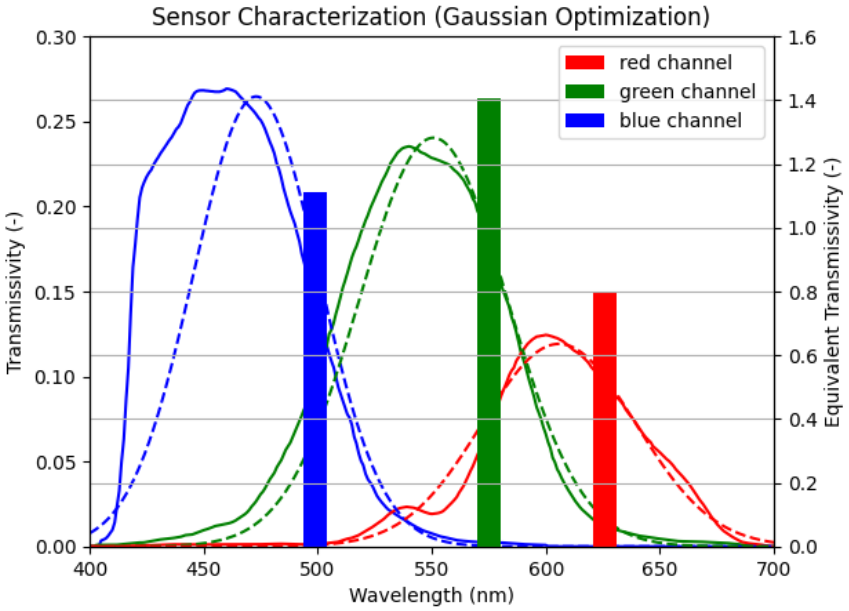

Figure 8. Prescribed spectral response (solid line), optimized Gaussian profile (dash line), and equivalent wavelength (bar) of the RGB color channel

Similar to the equivalent wavelength method, the optimized Gaussian profile is plugged into Equation 10 to calculate the signal intensity ratio of the blue/green, blue/red, and green/red pairs. The prescribed spectral response (real filter) is also plugged in Equation 10 and marked as dotted lines. It is seen that across the explored temperature range, the Gaussian profile method performs better than the equivalent wavelength method. Also, take the G/R channel as an example, the temperature is off by about 10 °C when the G/R ratio is 0.9. For soot in flames, the calculated Gaussian profile is plugged into Equation 11 to calculate the signal intensity ratio of the blue/green, blue/red, and green/red pairs. The results are marked as a dashed line in Figure 10.

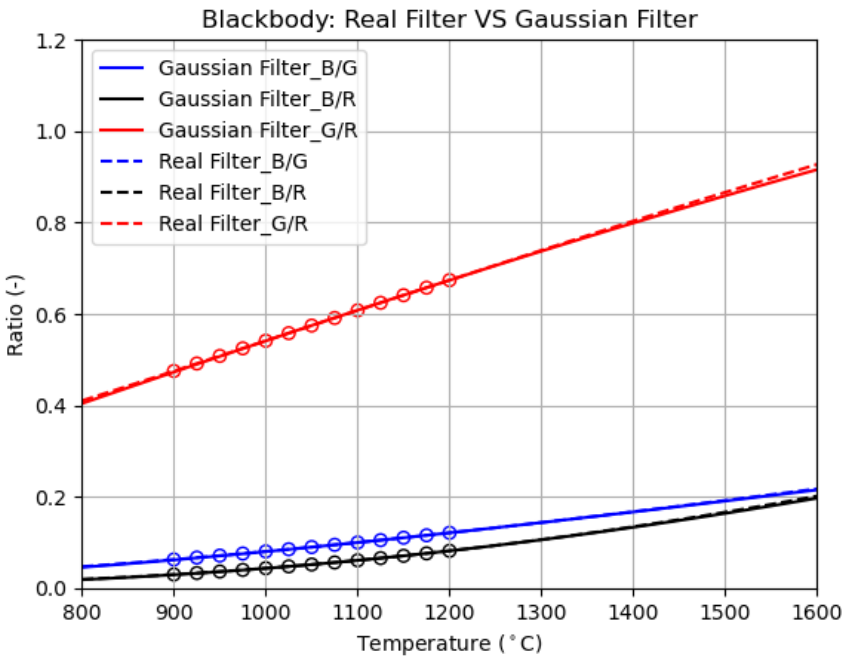

Figure 9. Correlation of blackbody furnace temperature with channel signal ratio using prescribed spectral response (dash line) and Gaussian profile (solid line)

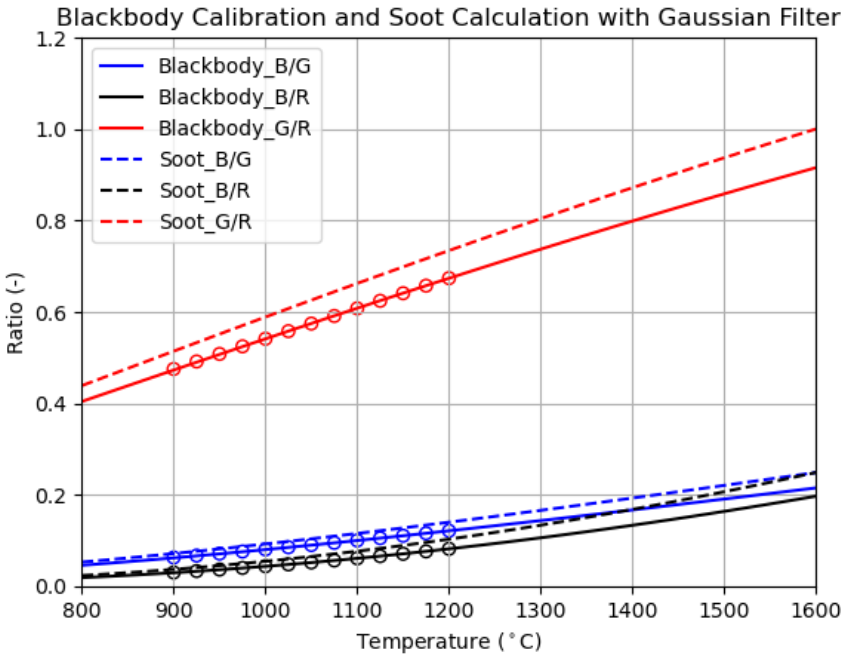

Figure 10. Correlation of blackbody furnace temperature (and soot temperature) with channel signal ratio using the Gaussian profile method

Overall, the Gaussian profile method performs the best among all three methods (inversed method, equivalent wavelength method, and Gaussian profile method) because it is least sensitive to signal noise and more accurate at higher temperatures.

4.3 Calculation of detector spectral response

The above simulation practice deals with a virtual imaging system that has a known spectral response. In dealing with the real blackbody calibration data, the spectral response of the detector is often not known. Both the equivalent wavelength method and the Gaussian profile method are used to calculate the digital camera's spectral response from the measured blackbody irradiance at each color channel.

4.3.1 Equivalent wavelength method

The developed equivalent wavelength method is implemented on the measured blackbody irradiance at each channel. Figure 11 plots the relative standard deviation of equivalent transmissivity among 13 blackbody furnace temperature settings using the measured blackbody irradiance. The correlation of blackbody furnace temperature (and soot temperature) with channel signal ratio using Equations 10 and 11 are summarized in Figure 12.

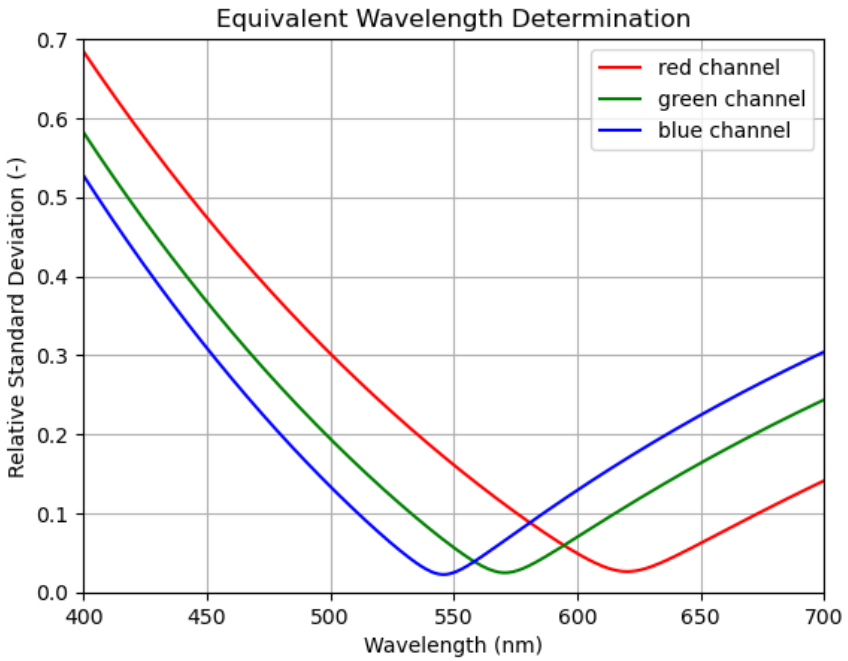

Figure 11. Relative standard deviation of the equivalent filter transmissivity using the measured blackbody irradiance

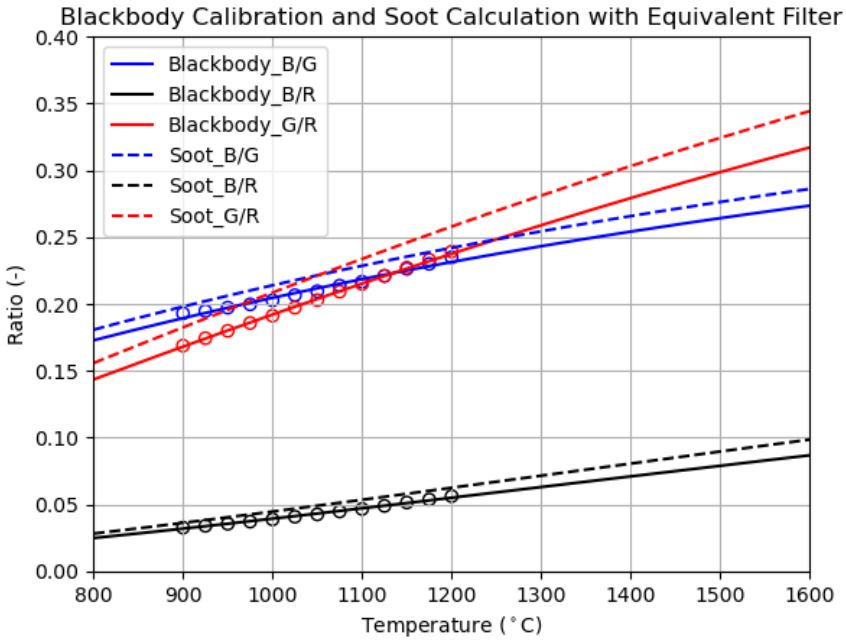

Figure 12. Correlation of blackbody furnace temperature (and soot temperature) with channel signal ratio using the equivalent wavelength method and the measured blackbody irradiance

4.3.2 Gaussian profile method

The developed equivalent wavelength method is implemented on the measured blackbody irradiance at each channel.

Figure 13 shows the calculated spectral response with the Gaussian profile method and the equivalent wavelength of each color channel. The correlation of blackbody furnace temperature (and soot temperature) with channel signal ratio using Equations 10 and 11 are summarized in Figure 14.

As discussed in the simulation section, the performance of the equivalent wavelength method deteriorates at higher temperature regions. In this research, the spectral response calculated using the Gaussian profile method is used for flame temperature and soot volume fraction measurement. The correlation of soot temperature with G/R signal intensity ratio in Figure 14 (red dash line) is used as the lookup table for flame temperature measurement.

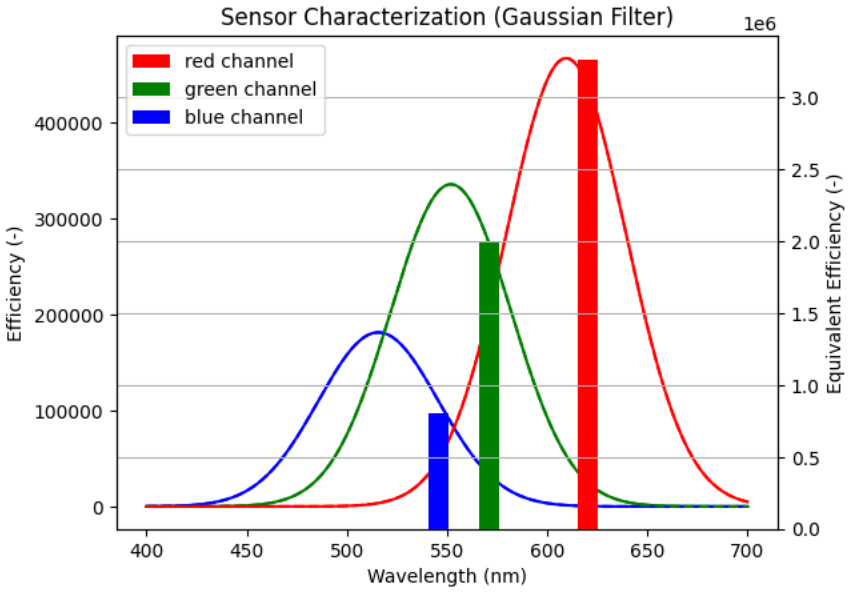

Figure 13. Comparison of the calculated Gaussian profile and the calculated equivalent wavelength using the measured blackbody irradiance

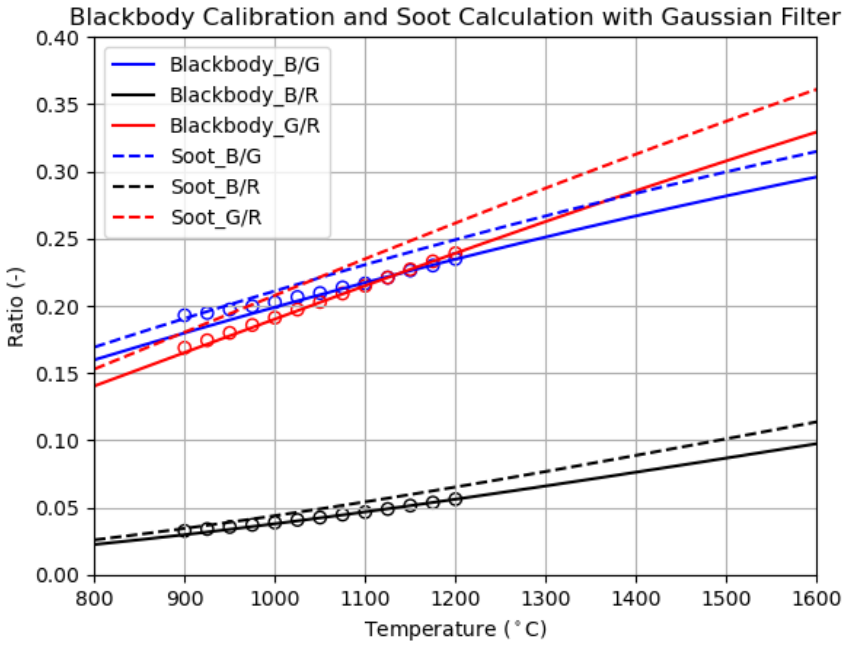

Figure 14. Correlation of blackbody furnace temperature (and soot temperature) with channel signal ratio using the Gaussian profile method and the measured blackbody irradiance

5 Results

The new camera technique is used to measure the flame temperature and soot volume fraction inside the developed flame system (MMA flame and MMA+TMP flame). This section presents the details of the measured flame temperature and soot volume fraction. Flame-retardant materials' impact on the flame structure is also discussed in this section.

5.1 Flame system

Color images of the MMA flame (left) and MMA+TMP flame (right) are shown in Figure 15. Gamma correction is removed, and each color channel is below its saturation level. The tip of the wick is marked as a white dashed line. The flame is laminar, axisymmetric, and steady for more than 30s. The MMA flame tip sharpens as fuel burns out. Soot oxidation is sufficient, allowing soot to be confined within the combustion region. No soot emits out of the MMA flame. Flame diameter is broadened when mixed with TMP flame-retardant material. In the MMA+TMP flame, no obvious sharpening on the flame tip is observed. Flame tip breaks with soot emits out of the combustion zone.

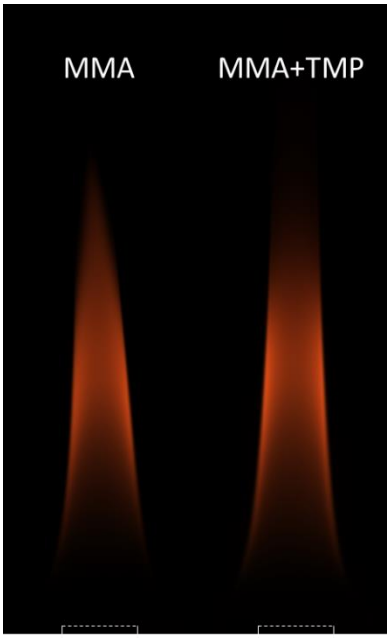

Figure 15. Color photo of the MMA flame (left) and the MMA+TMP flame (right)

5.2 Deconvolution results

This section displays the original projected signal intensity and the deconvolved signal intensity. The original projected intensity is confirmed to be axisymmetric, so the left and the right side (about the center axis) of the intensities are averaged. Only the averaged results are shown. Deconvolution of the averaged intensity is performed using Equation 17.

5.2.1 MMA flame

Figure 16 - Figure 19 show the projected (left side) and deconvolved (right side) signal intensity at representative heights (10, 20, 30, and 40 mm) of the MMA flame. It is seen that after deconvolution, the irradiance has its peak at its outer radius. This is because in diffusion flames, a chemical reaction is fasted at the flame sheet where the fuel/air ratio is stoichiometric. The fuel is rich as it is closer towards the flame center, and is lean as it is closer to the outer ambient condition. On either side, the chemical reactions that involve soot formation are also significantly suppressed. Near the center at a flame height of 10 mm, the soot irradiance is almost zero because there is not much soot produced and flame temperature is low.

Flame diameter decreases as the flame height increases. At a height of 30 mm, there is enough air entrained to support soot formation. A considerable amount of soot irradiance near the center can also be observed. At a flame height of 40 mm, soot irradiance peaks at the centerline.

It is noted that the numerical error accumulates as it moves towards the centerline during deconvolution. Therefore, the deconvolved signal has a higher noise level near the centerline, as shown in the figures below.

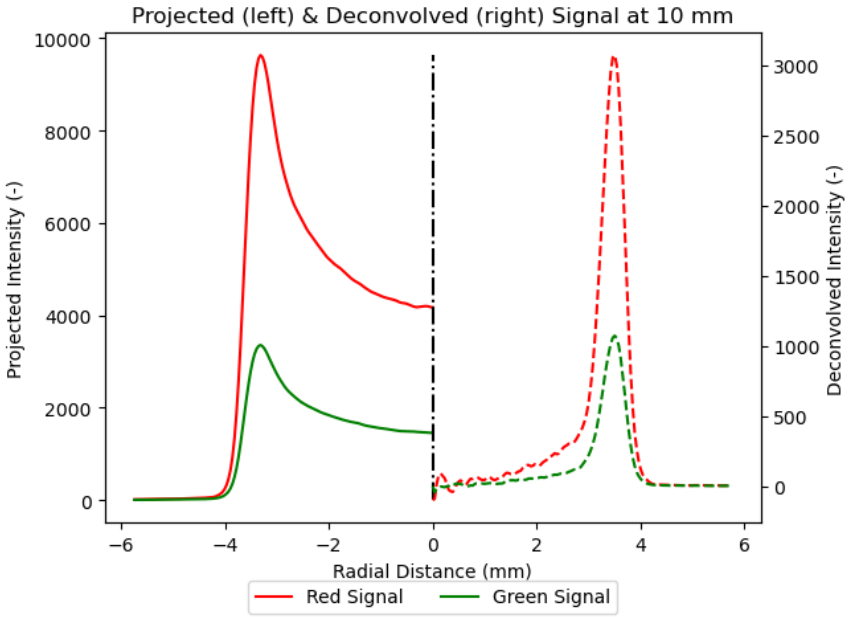

Figure 16. Projected (left) and deconvolved (right) red and green channel signal intensity of MMA flame at 10-mm flame height

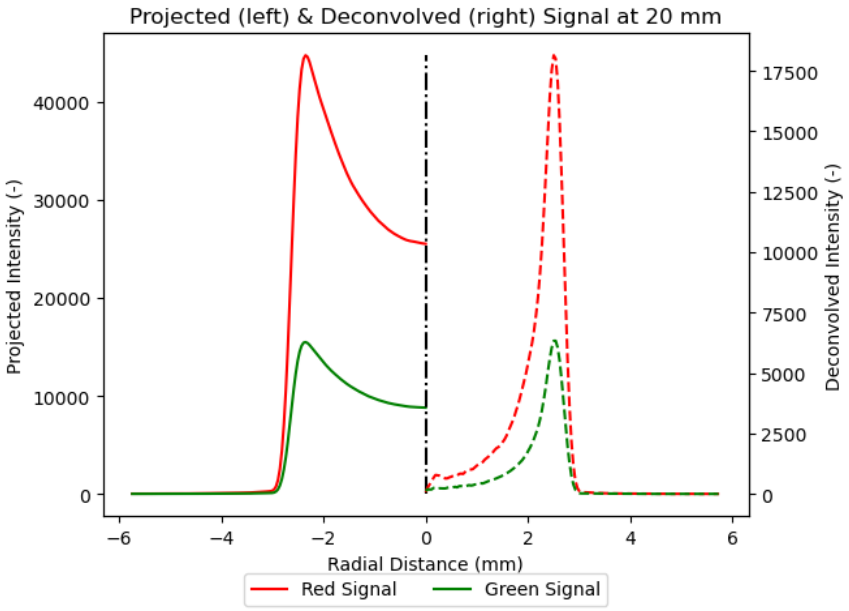

Figure 17. Projected (left) and deconvolved (right) red and green channel signal intensity of MMA flame at 20-mm flame height

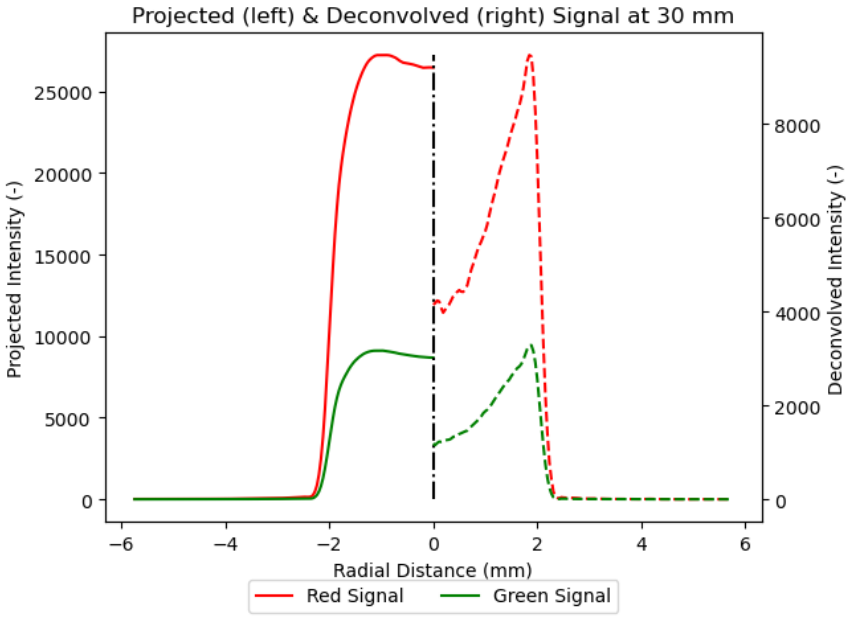

Figure 18. Projected (left) and deconvolved (right) red and green channel signal intensity of MMA flame at 30-mm flame height

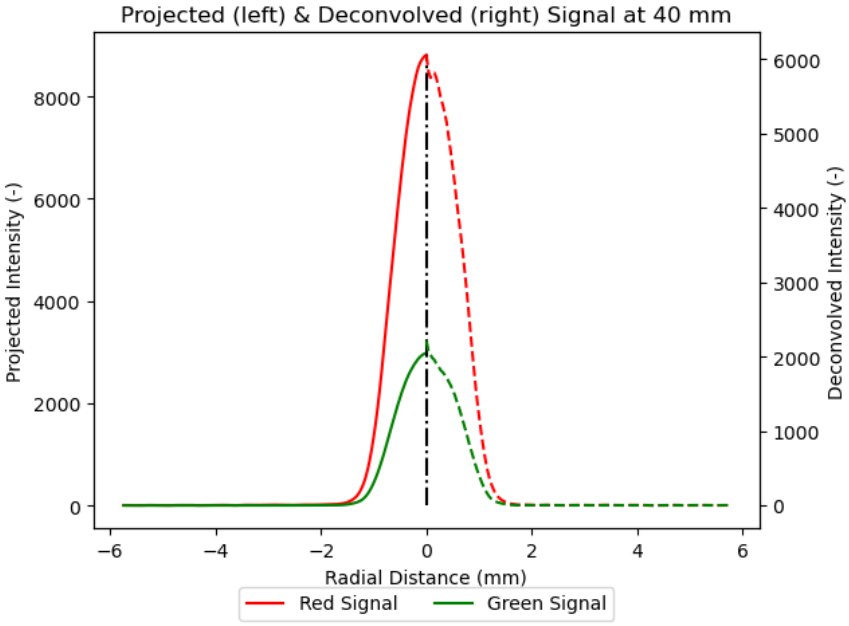

Figure 19. Projected (left) and deconvolved (right) red and green channel signal intensity of MMA flame at 40-mm flame height

5.2.2 MMA + TMP flame

Figure 20 - Figure 23 show the projected (left side) and deconvolved (right side) signal intensity at representative heights (10, 20, 30, and 40 mm) of the MMA+TMP flame. Phenomena similar to the MMA flame can be observed. At 40 mm height, soot irradiance is still the strongest near the outer radius.

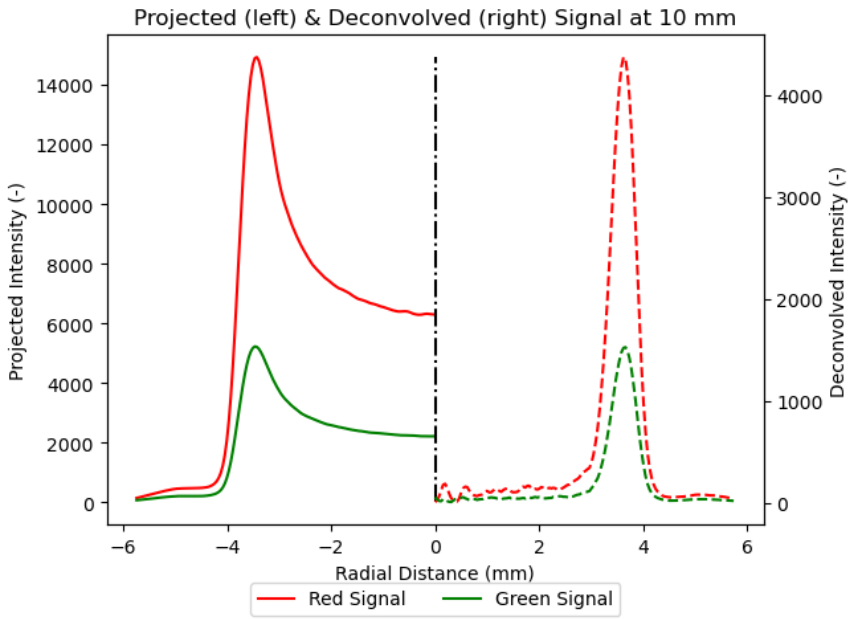

Figure 20. Projected (left) and deconvolved (right) red and green channel signal intensity of MMA+TMP flame at 10-mm flame height

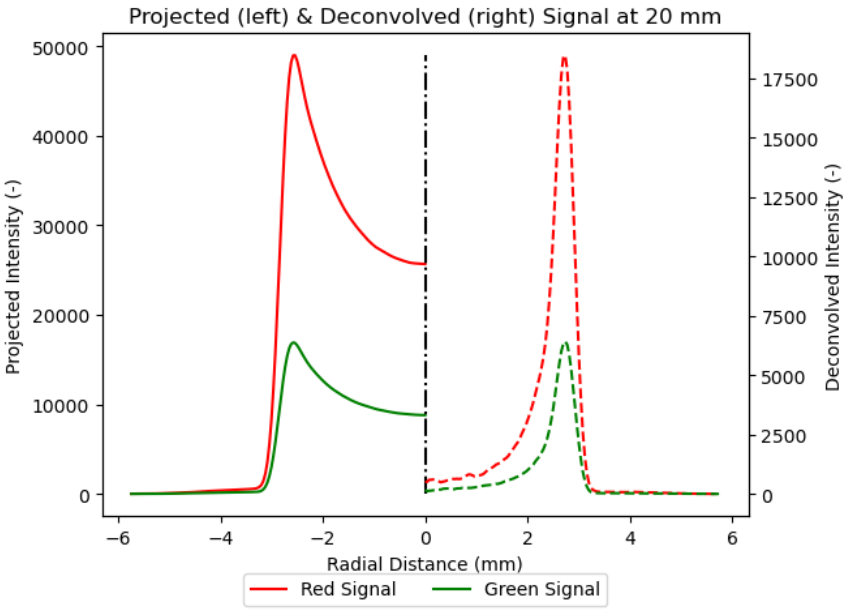

Figure 21. Projected (left) and deconvolved (right) red and green channel signal intensity of MMA+TMP flame at 20-mm flame height

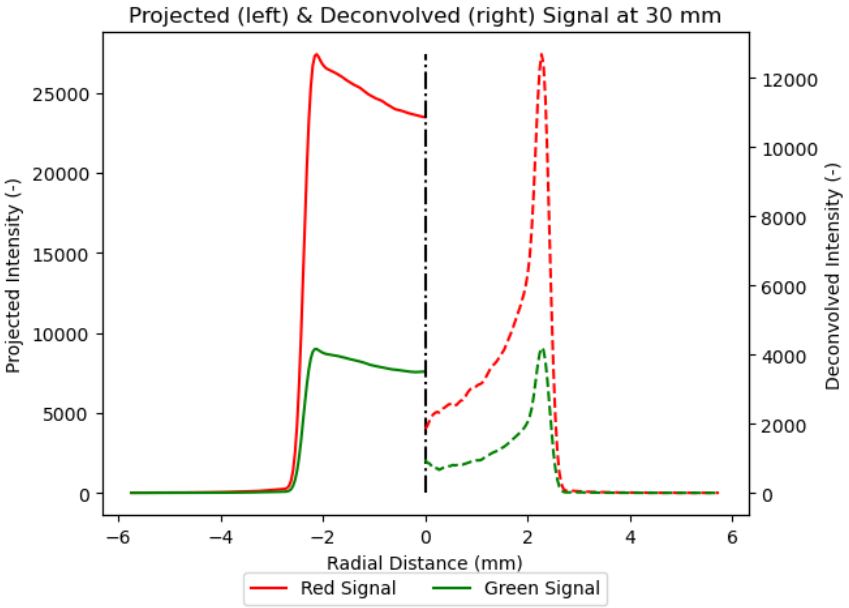

Figure 22. Projected (left) and deconvolved (right) red and green channel signal intensity of MMA+TMP flame at 30-mm flame height

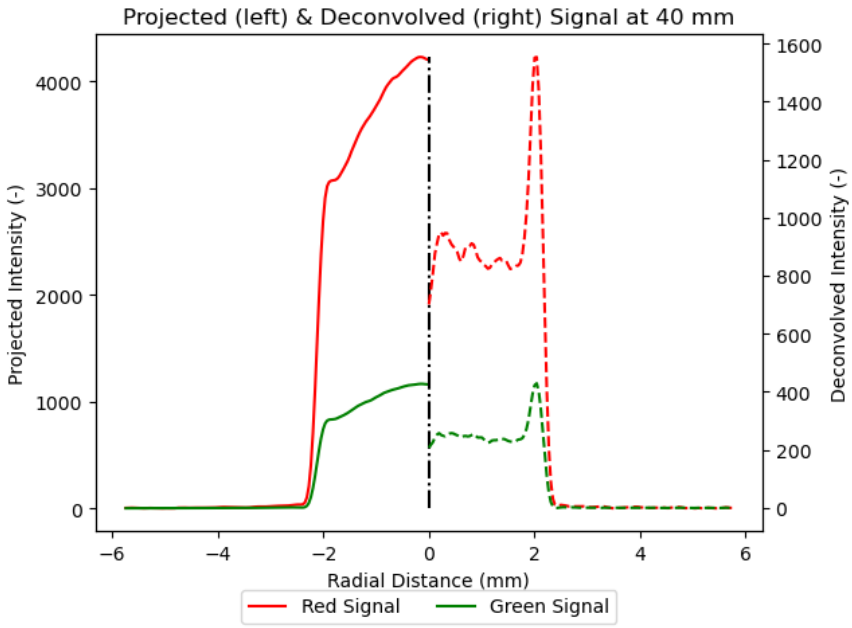

Figure 23. Projected (left) and deconvolved (right) red and green channel signal intensity of MMA+TMP flame at 40-mm flame height

5.3 Temperature and soot volume fraction

The ratios of the green and red channel signal can be calculated, and its corresponding temperature can be determined from the correlation established in Figure 14 (red dash line). Due to higher noise level and negligible soot irradiance near the flame centerline, temperatures with local irradiance lower than 20% of the maximum value are discarded. The ratio of the projected signal (not deconvolved) is also calculated, and its corresponding temperature is also presented. It should be noted that temperature calculated from a projected signal without deconvolution does not have a rigorous physical meaning and is just for reference.

Ideally, the local soot volume fraction should be calculated using the deconvolved signal intensity $I(r)$ and the temperature with deconvolved signal $T(r)$. In this research, $T(r)$ near flame centerline has a high noise level and is discarded. Instead, the deconvolved signal intensity $I(r)$ coupled with temperature with projected signal $T(x)$ is used.

5.3.1 MMA flame

Figure 24 - Figure 27 display the calculated flame temperature $T(r)$ using deconvolved signal $I(r)$, the calculated flame temperature $T(x)$ using projected signal $I(x)$, and the soot volume fraction using $I(r)$ and $T(x)$ at representative heights (10, 20, 30, and 40 mm) of the MMA flame.

The initial soot column has an annular shape. Center soot volume fraction increases as more air is entrained and flame diameter is narrowed. Near the region with sufficient soot (for irradiance emission), $T(r)$ agrees well with $T(x)$. At each flame height, both $T(r)$ and $T(x)$ peaks near the flame sheet (outer radius).

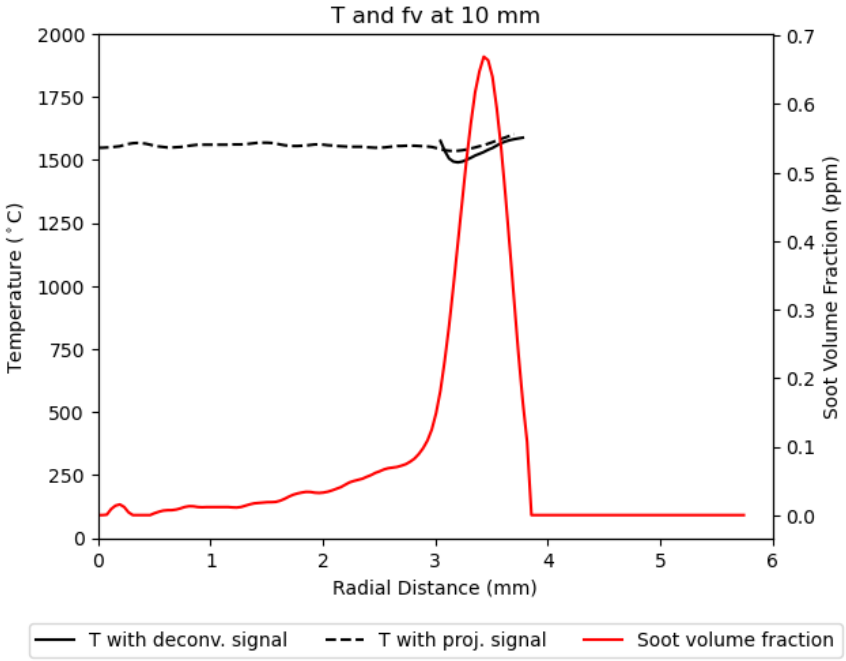

Figure 24. Measured MMA flame temperature using deconvolved signal (black solid) and projected signal (black dash), and soot volume fraction (red solid) at 10-mm flame height

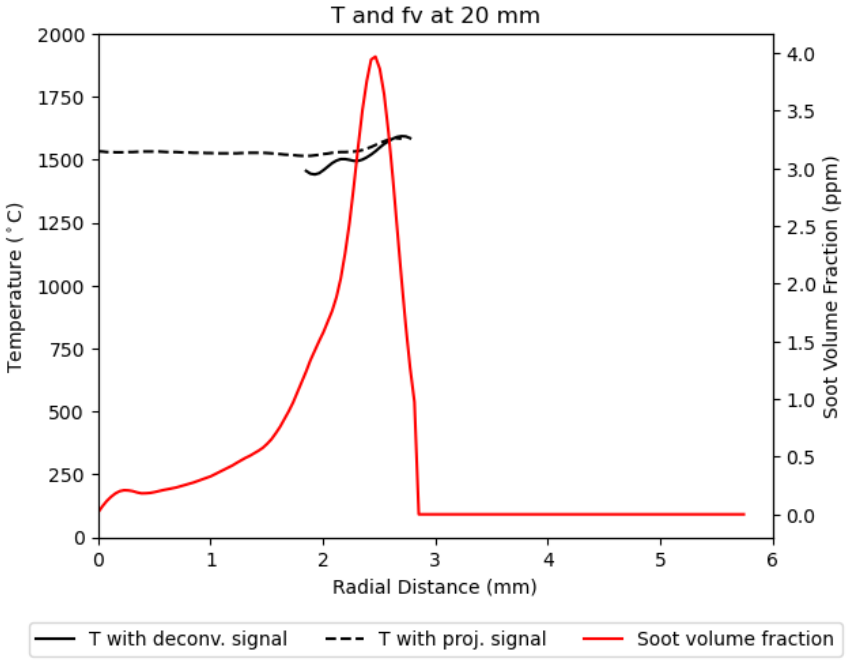

Figure 25. Measured MMA flame temperature using deconvolved signal (black solid) and projected signal (black dash), and soot volume fraction (red solid) at 20-mm flame height

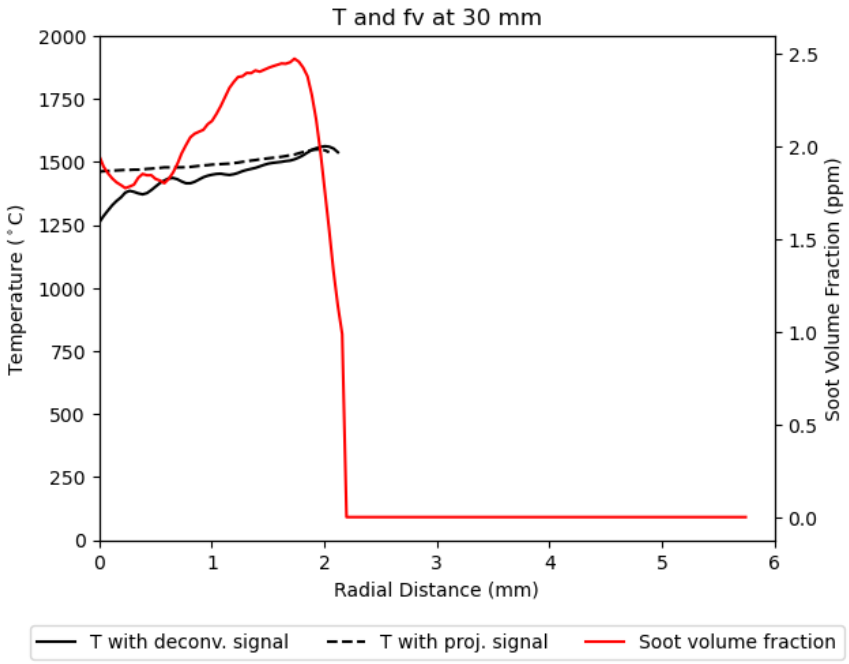

Figure 26. Measured MMA flame temperature using deconvolved signal (black solid) and projected signal (black dash), and soot volume fraction (red solid) at 30-mm flame height

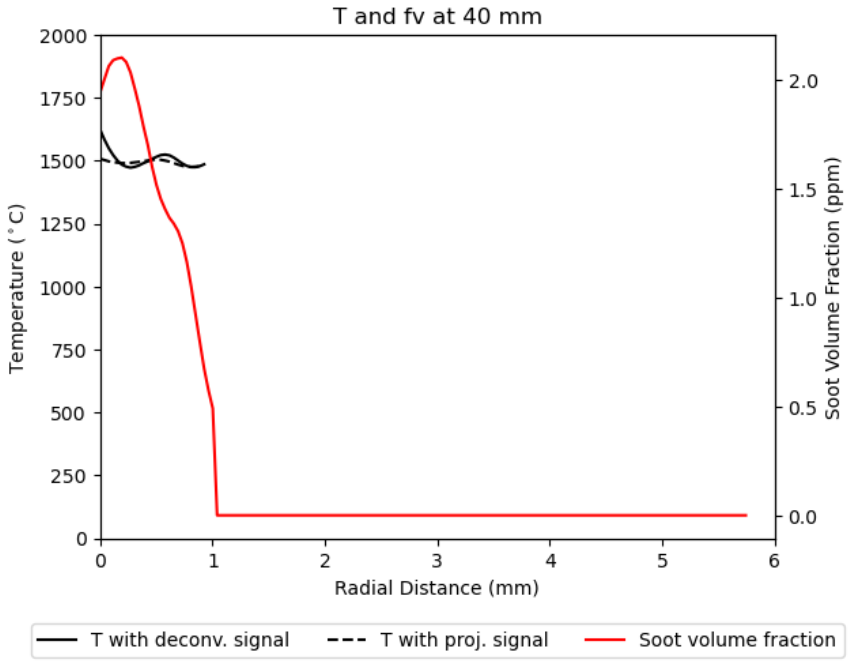

Figure 27. Measured MMA flame temperature using deconvolved signal (black solid) and projected signal (black dash), and soot volume fraction (red solid) at 40-mm flame height

5.3.2 MMA + TMP flame

Figure 28 - Figure 31 display the calculated flame temperature $T(r)$ using deconvolved signal $I(r)$, the calculated flame temperature $T(x)$ using projected signal $I(x)$, and the soot volume fraction using $I(r)$ and $T(x)$ at representative heights (10-, 20-, 30-, and 40-mm) of the MMA+TMP flame.

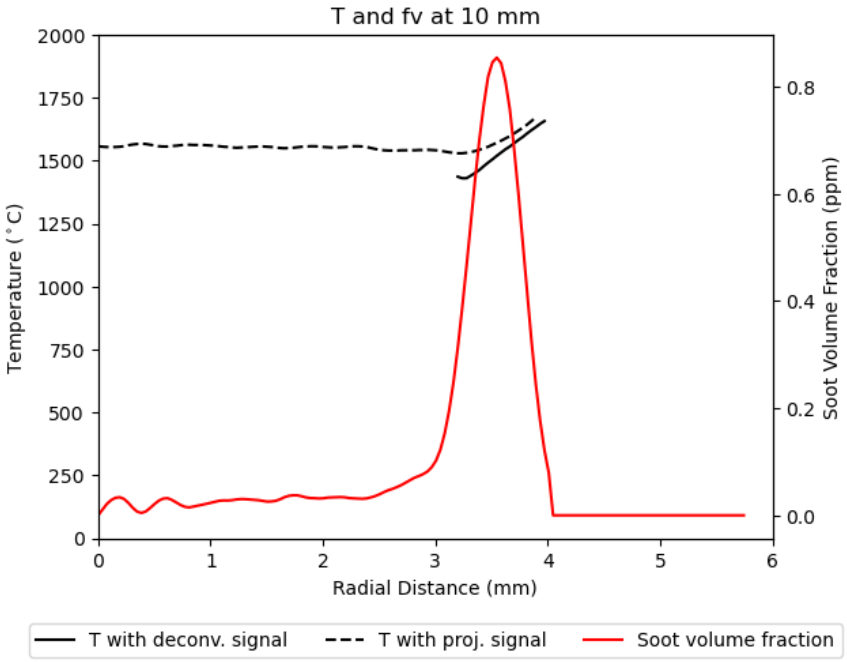

Figure 28. Measured MMA+TMP flame temperature using deconvolved signal (black solid) and projected signal (black dash), and soot volume fraction (red solid) at 10-mm flame height

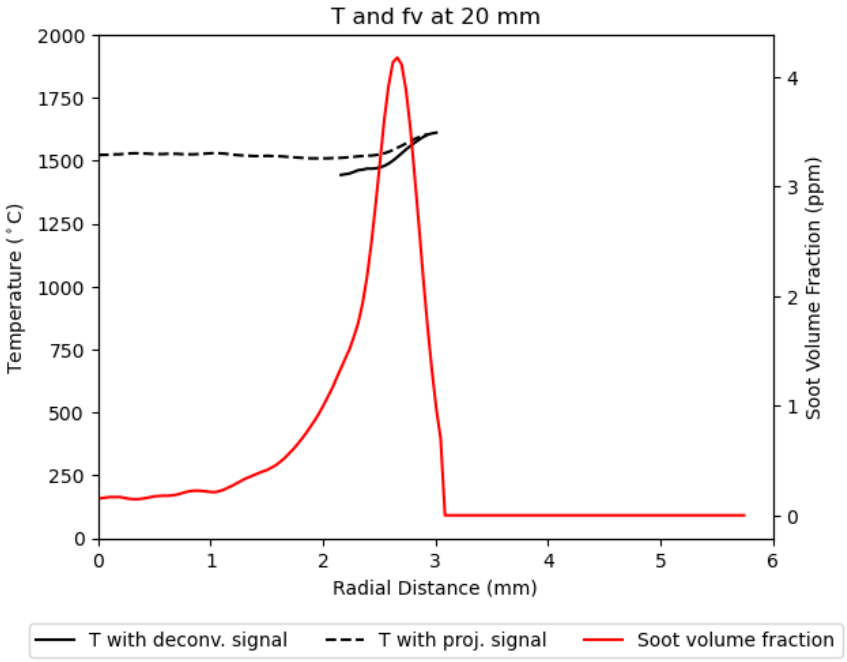

Figure 29. Measured MMA+TMP flame temperature using deconvolved signal (black solid) and projected signal (black dash), and soot volume fraction (red solid) at 20-mm flame height

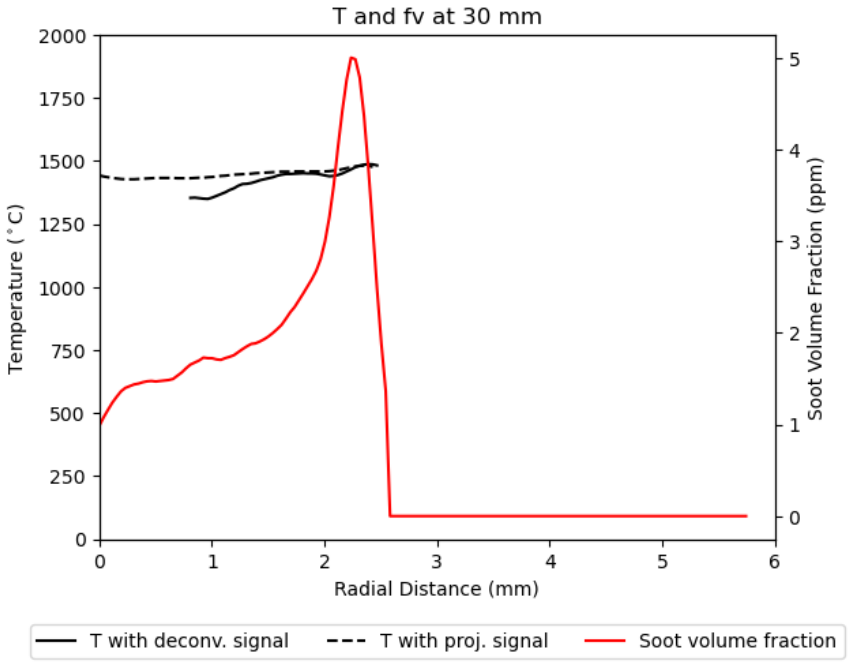

Figure 30. Measured MMA+TMP flame temperature using deconvolved signal (black solid) and projected signal (black dash), and soot volume fraction (red solid) at 30-mm flame height

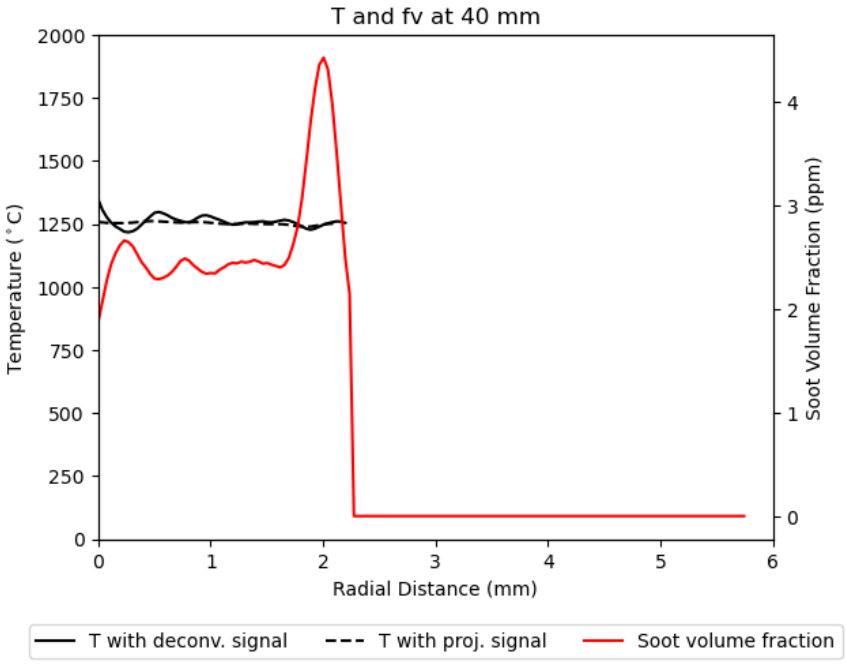

Figure 31. Measured MMA+TMP flame temperature using deconvolved signal (black solid) and projected signal (black dash), and soot volume fraction (red solid) at 40-mm flame height

5.3.3 Contour results

The detailed radially-distributed flame temperature and soot volume fraction at each height (1 mm increment) is combined to generate the contour plot of temperature and soot volume fraction. The temperature contour plots of the MMA flame and the MMA+TMP flame are summarized in Figure 32 and Figure 33. The shape of the contour is stretched radially to reveal more details inside the flame. In both flames, the flame temperature near the bottom center is discarded due to insufficient soot to emit irradiance. Temperature peaks at the flame sheet near the outer radius. The flame-retardant material does not have a noticeable impact on the flame sheet temperature below 25-mm flame height. Above 25-mm flame height, the flame sheet of the MMA flame can maintain that high temperature whereas, in the MMA+TMP flame, the temperature quickly decreases. Near the flame centerline, MMA flame temperature can maintain higher than 1450 °C; while MMA+TMP flame temperature decreases significantly to 1250 °C,

which is closer to the flame extinction temperature of 1300 °C reported by Quintiere et al. (Quintiere, 2006).

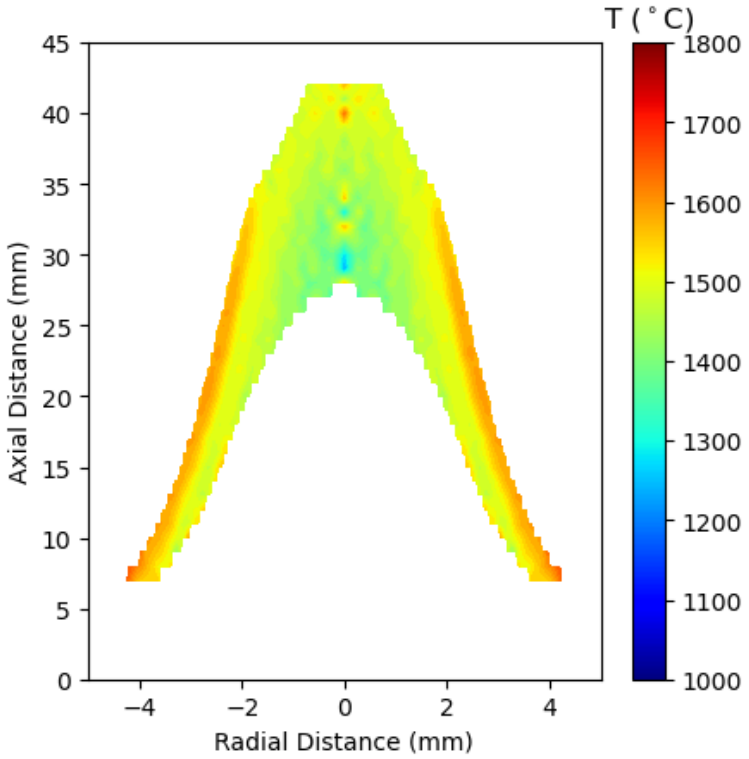

Figure 32. Contour plot of MMA flame temperature

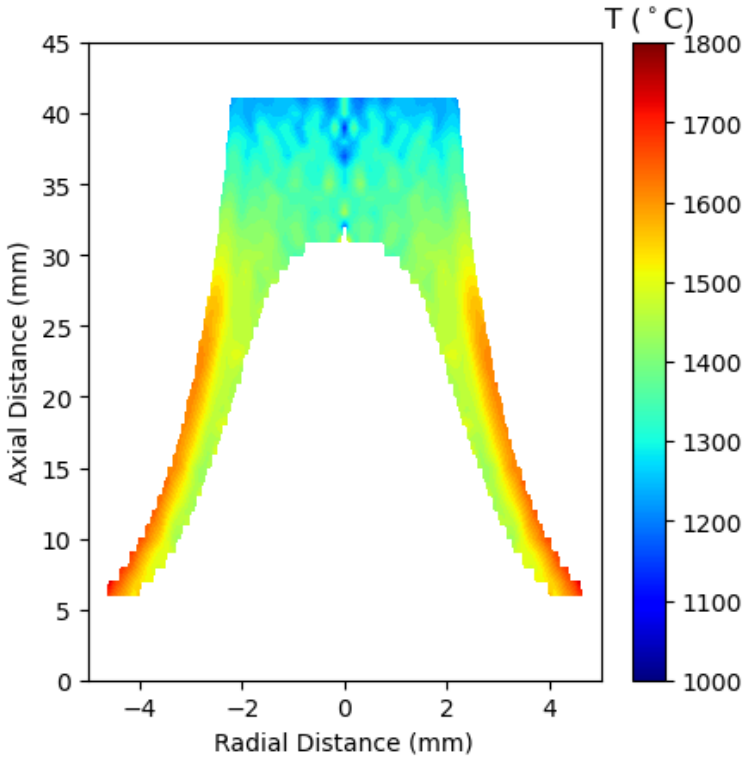

Figure 33. Contour plot of MMA+TMP flame temperature

The soot volume fraction contour plots of the MMA flame and the MMA+TMP flame are summarized in Figure 34 and Figure 35. The shape of the contour is also stretched radially to reveal more details inside the flame. Both flames have a peak volume fraction at the outer radius, as indicated in the figures. In the MMA flame at the outer radius, soot grows and peaks at 22 mm height, having a peak soot volume fraction of about 4.5 ppm. The soot volume fraction then decreases with height as soot oxidation becomes larger than soot formation. In the MMA+TMP flame at outer radius, soot peaks at about 30 mm height, having a peak soot volume fraction of about 5.5 ppm. Beyond that, there is no obvious reduction in the soot volume fraction. The centerline soot volume fraction also increases continuously at upper height. It appears that the soot oxidation is suppressed. According to the experimental findings by Guo et al. (Guo, Walters, Lyon, & Crowley, 2021), phosphorus-containing flame retardant is directly incorporated into soot's structure and decreases its surface reactivity. At the tip of the MMA+TMP flame, there is a substantial amount of soot volume fraction (2 - 4 ppm) when the flame is extinguished.

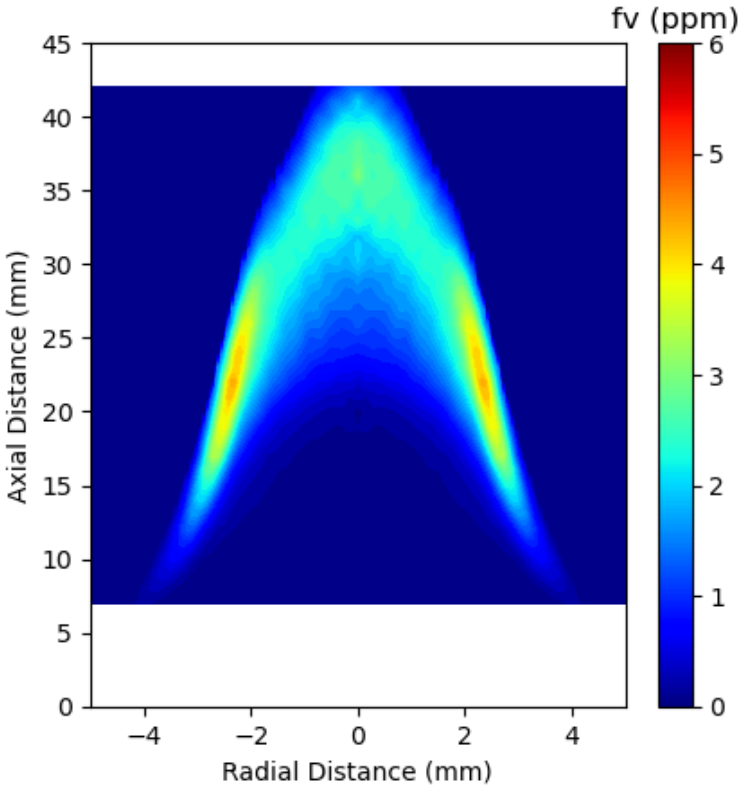

Figure 34. Contour plot of MMA flame soot volume fraction

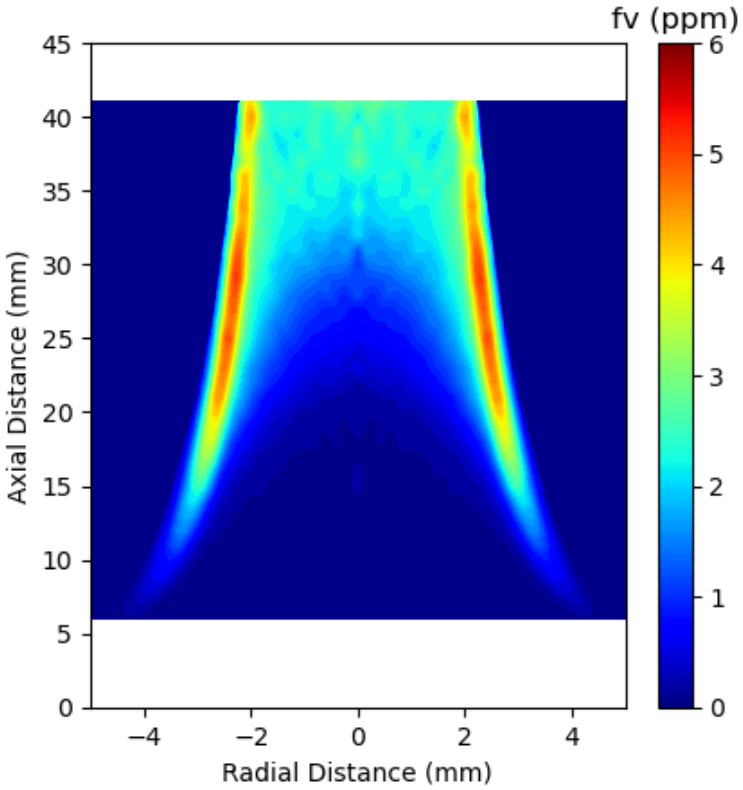

Figure 35. Contour plot of MMA+TMP flame soot volume fraction

6 Discussions

The soot volume fraction can be integrated across the flame cross-section area to better visualize the soot evolution (formation and oxidation) inside the flame:

$$F_v = \int_0^R 2\pi r f_v(r) dr \tag{23}$$

Integration over the multiplying of f_v by soot density ρ_s and gas velocity v yields the soot mass flux at each height (Guo, 2015).

$$\dot{m}_s = \rho_s \int_0^R 2\pi r f_v(r) v(r) dr \tag{24}$$

Unfortunately, the gas velocity is not directly measured in the current research. Here for simplification, it is assumed that gas velocity does not change in the explored radial and axial direction; and flame retardant does not have an impact on the flame velocity. Integrated soot

volume fraction F_v can represent the soot mass flux information. The calculated results are summarized in Figure 36.

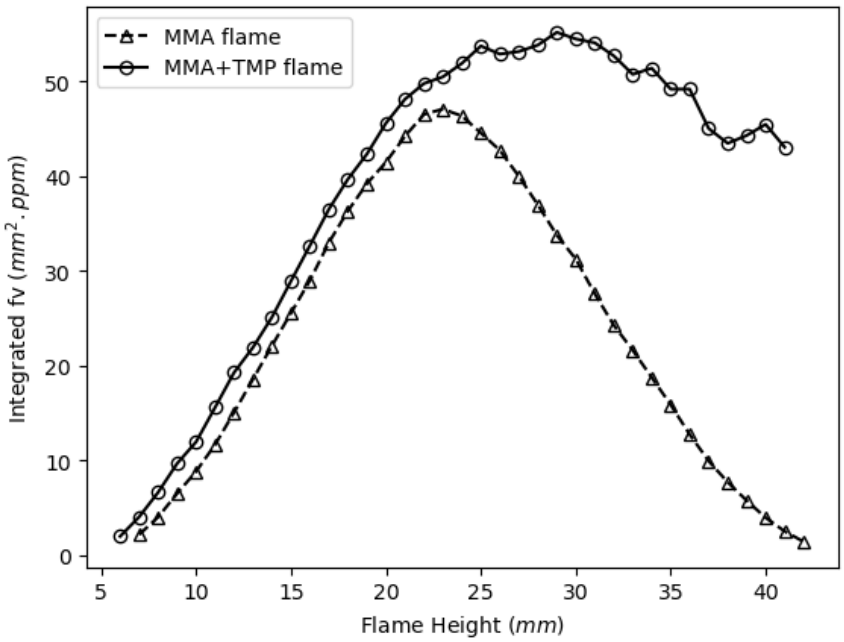

Figure 36. Integrated soot volume fraction at different heights for MMA and MMA+TMP flame

Below the flame height of 22 mm, F_v in both flames has a similar trend. F_v of the MMA+TMP flame is slightly higher than that of the MMA flame. Above 22 mm, F_v of the MMA flame drastically decreases as height increases. Soot is almost completely oxidized at a flame height of 40 mm. On the contrary, F_v of the MMA+TMP flame only decreases by about 20% at the flame height of 40 mm.

In comparing the flame structure (shape, flame temperature, and soot volume fraction) between the MMA flame and the MMA+TMP flame, the difference at lower flame heights is relatively small. According to the research by Guo et al. (Guo, Lyon, Safronava, Walters, & Crowley, 2018), phosphorus as a flame retardant does not have much impact on the homogenous gas-phase chemical reaction. A major difference occurs at an upper height of the flame region where soot oxidation starts to take place. According to the research by Guo et al. (Guo, Walters, Lyon, & Crowley, 2021), flame retardancy also reduces the soot surface reactivity that suppresses oxidation. The promoted soot formation at lower heights and suppressed soot oxidation at upper heights result in an increased level of soot concentration in the MMA+TMP flame. The increased soot level (see Figure 34 and Figure 35) serves as a good radiation emitter which further decreases the flame temperature (see Figure 32 and Figure 33).

7 Conclusions

In this research, a digital camera was used as a pyrometer for high-fidelity flame temperature and soot volume fraction measurements. The imaging system was simultaneously calibrated and characterized with a blackbody furnace to obtain optical constants, spectral response, and linearity of the imaging system. Deconvolution was performed on the line-of-sight integrated signal to reconstruct the local soot irradiance. A Python-based toolbox was developed to automatically scan the flame image, perform subsequent imaging-processing steps, and calculate the corresponding flame temperature and soot volume fraction. The newly developed technique allows the detailed distribution of the flame temperature and the soot volume fraction to be accurately measured with a single photo.

The camera technique was implemented on a liquid-fueled (liquid methyl methacrylate (MMA) laminar diffusion flame to reveal the impact of phosphorus-containing flame-retardant material on the chemical kinetics within the fire. In this flame system, 2% (m/m) of trimethyl phosphate (TMP) is mixed with MMA. It was found that at a lower flame height where soot formation normally occurs, the MMA+TMP flame involves a slightly higher rate of soot formation. At upper heights where soot oxidation normally occurs, TMP significantly suppresses soot oxidation. The soot concentration level at the upper height of the MMA+TMP flame is significantly higher than that of the pure MMA flame. The increased soot level results in much higher energy radiation that cools the local flame temperature. As a result, the flame extinguishes before fuel is completely burned and soot emits out of the flame tip.

8 Bibliography

Coffin, D. (2021). *Decoding raw digital photos in Linux*. Retrieved from https://www.dechifro.org/dcraw/

Dalzell, W. H., Williams, G. C., & Hottel, H. C. (1970). A lightscattering method for concentration measurements. *Combustion and Flame, 14*, 161-169.

Guo, H. (2015). *Soot Oxidation in Hydrocarbon-free flames.* College Park: University of Maryland College Park.

Guo, H., Castillo, J. A., & Sunderland, P. B. (2013). Digital camera measurements of soot temperature and soot volume fraction in axisymmetric flames. *Applied Optics, 52*, 8040-8047.

Guo, H., Lyon, R. E., Safronava, N., Walters, R. N., & Crowley, S. (2018). A simplified model on carbon monoxide yield in burning of polymeric solids containing flame retardants. *Fuel, 222*, 175-179.

Guo, H., Walters, R. N., Lyon, R. E., & Crowley, S. (2021). Effect of phosphorus on soot formation and flame retardancy in fires. *Fire Safety Journal, 120*, 103068.

Hughey, B. J., & Santavicca, D. A. (1982). A comparison of techniques for reconstructing axisymmetric reacting flow fields from absorption measurements. *Combustion Science and Technology, 29*, 167-190.

Korobeinichev, O. P., Bolshova, T. A., Shvartsberg, V. M., & Chernov, A. A. (2001). Inhibition and Promotion of Combustion by Organophosphorus Compounds Added to Flames of CH4 or H2 in O2 and Ar. *Combustion and Flame, 125*, 744-751.

Kuhn, P. B., Ma, B., Connelly, B. C., Smooke, M. D., & Long, M. B. (2011). Soot and thin-filament pyrometry using a color digital camera. *Proceedings of the Combustion Institute, 33*, 734-750.

Marker, T. R. (2019). *Aircraft Materials Fire Test Handbook, Revision 3.* U.S. Department of Transportation, Federal Aviation Administration.

Maun, J. D., Sunderland, P. B., & Urban, D. L. (2007). Thin-filament pyrometry with a digital still camera. *Applied Optics, 46*, 483-488.

Quintiere, J. (2006). *Fundamentals of Fire Phenomena.* John Wiley & Sons, Ltd.

Raffan-Montoya, F., Ding, X., Stoliarov, S. I., & Kraemer, R. H. (2015). Measurement of heat release in laminar diffusion flames fueled by controlled pyrolysis of milligram-sized solid samples: Impact of bromine- and phosphorus-based flame retardants. *Combustion and Flame, 162*, 4660-4670.

Shaddix, C. R. (2017). A new method to compute the proper radiant heat transfer correction of bare-wire thermocouple measurements. *10th U. S. National Combustion Meeting*, (p. 6).

Snelling, D. R., Thomson, K. A., Smallwood, G. J., & Gulder, O. L. (2002). Spectrally resolved measurement of flame radiation to determine soot temperature and concentration. *AIAA Journal, 40*, 1789–1795.